RESPONSE ANALYSIS OF THE FLOW-INDUCED VIBRATION OF FLEXIBLE CYLINDERS TESTED AT CASTINE, MAINE IN JULY AND AUGUST OF 1981

by

JEN-YI JONG
J. KIM VANDIVER
DEPARTMENT OF OCEAN ENGINEERING
MASSACHUSETTS INSTITUTE OF TECHNOLOGY
CAMBRIDGE, MASS. 02139

15 January 1983

ABSTRACT

A cable-strumming experiment was conducted at Castine, Maine in July and August of 1981. 75-foot long sections of a 1.25-inch diameter cable, and a 1.631-inch diameter pipe were subjected to vortex induced vibration. Seven biaxial pairs of accelerometers were placed at different locations along the cable, and the pipe. Acceleration at these seven positions, as well as tension, tidal current velocity, and drag force were simultaneously recorded. Current velocities ranged from 0 to 2.4 feet/second. A numerical double integration technique is presented in detail and used to obtain the transverse and in-line displacements. Modal identification is used to evaluate the motion in terms of the individual natural modal coordinates of the cable. Lockin and non-lockin examples are presented. Cross flow amplitudes are typically twice that of the in-line vibration. In-line response frequencies are typically twice that of the cross flow.

ACKNOWLEDGEMENTS

This research was part of a joint industry and government sponsored project by the American Bureau of Shipping, Brown and Root, Inc., Chevron Oil Field Research, Conoco, Inc., Exxon Production Research, Shell Development Company, Union Oil Research, the Office of Naval Research, and the Naval Civil Engineering Laboratory, and the U.S. Geological Survey.

An eight member team led by Professor J. Kim Vandiver participated in the field experiments. Prof. Vandiver was assisted during these experiments by Charles Mazel, Jen-Yi Jong, Ed Moas, Peter Stein, Mark Whitney, Pam Vandiver, and Jim McGlothlin.

TABLE OF CONTENTS

LIST OF FIGURES

LIST OF FIGURES

CHAPTER 1
INTRODUCTION

Marine risers, tension elements on TLP's, and hydrophone cables are all examples of structures subject to vortex-induced vibration. The response of the cylinder depends upon a complex interaction between the natural modes of the vibration and the vortex-shedding process.

The purpose of this research was to evaluate the in-line and cross-flow displacements of long flexible cylinders from acceleration data obtained in field tests. Individual modal amplitudes were to be determined for in-line and cross-flow response for both lock-in and non-lock-in conditions. Experiments were performed on long flexible cylinders 75 feet in length which were exposed to uniform current ranging from 0 to 2.4 feet/second. Measurements taken included current, drag, tension and biaxial acceleration at seven locations along the test cylinders.

The angular orientations of the biaxial accelerometers were initial unknowns which had to be resolved by evaluation of the gravitational acceleration components recorded with the data. Once the orientation was established the horizontal (in-line) and vertical (cross-flow) vector acceleration components were obtained. A numerical double integration technique was developed to determine the vector displacement time histories at the seven measurement locations. The theoretical mode shapes of uniform cables, and beams under tension, with pinned ends, are simple sinusoids. By a least squares error minimization technique, it was possible to evaluate the individual modal contributions for in-line and cross-flow motions, and for lock-in and non-lock-in conditions. In other words, the vector displacement response was reduced to the separate time histories of the natural coordinates of the individual contributing modes. The data processing methodologies are

described and typical results are presented. Two and one half hour records of drag coefficient, current, and RMS displacement were calculated and are presented.

CHAPTER 2
THE EXPERIMENT

2.1 Test Site

The site chosen for the experiment, shown in Fig. 1 was a sandbar located at the mouth of Holbrook Cove near Castine Maine. This was the same site used in previous experiments in 1975 and 1976 by Vandiver, Mazel and Kan (12,18). At low tide, the sandbar was exposed allowing easy access to the test equipment while at high tide it was covered by about 10 feet of water. The test section was oriented normal to the direction of the current which varied from 0 to 2.4 ft/s over the tidal cycle with only small spatial differences over the section length at any given moment.

The data taking station for the experiment was the R/V Edgerton chartered from the MIT Sea Grant Program. The Edgerton was moored for the duration of the experiment approximately 300 ft. from the sandbar and connected to the instruments on the sandbar by umbilicals.

Prior to the data taking part of the experiment, several days were needed to prepare the site. A foundation for the experiment was needed to anchor the supports that were to hold the ends of the test cylinders. To accomplish this, six 4.5 inch diameter steel pipes were water jetted into the sandbar utilizing the fire pump aboard the Edgerton. These six pipes were made of two, five foot sections joined by couplings so that the overall length of each was 10.0 feet. In addition, one 2.0 inch steel pipe, 6 feet long, was jetted into the sandbar to be used as a current meter mount. Fig. 2 shows a schematic diagram of the experiment test section.

2.2 Drag Measuring System

A load cell mounted at one end of the test cylinder measured the horizontal shear force on one end of the test cylinder. The cylinder and its supports were symmetric, and therefore the measured force was one half the total drag force on the cylinder. Mean drag force was measured. The

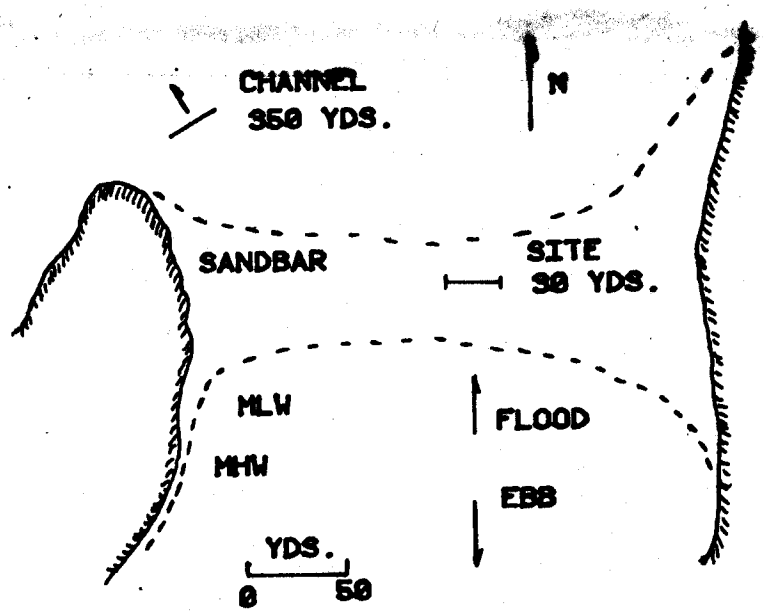

PLAN

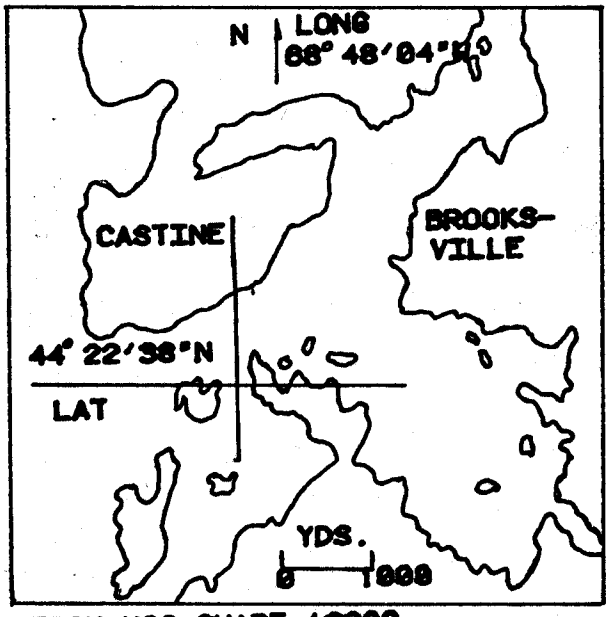

FROM NOS CHART 13309

FIG. 1 THE EXPERIMENT SITE

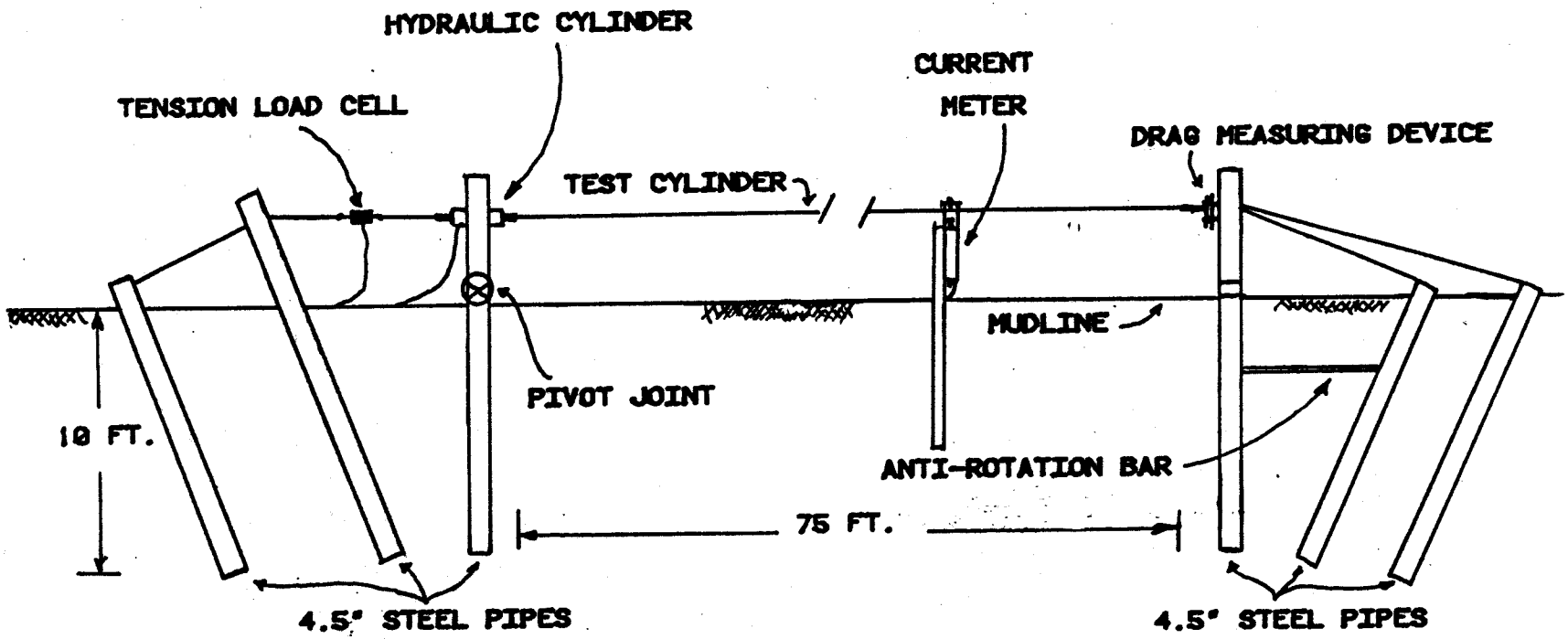

FIG. 2 SCHEMATIC DIAGRAM OF THE EXPERIMENT TEST SECTION

mechanical details of the drag measuring mechanism way be found in the thesis by J.McGlothlin. The load cell was a Sensotec Model 41, packaged for underwater use. The signal from the load cell traveled through wires in the test cylinders and through the umbilical to the Edgerton where it was conditioned and recorded.

2.3 Current Measuring System

The current was measured by a Neil Brown Instrument Systems DRCM -2 Acoustic Current Meter located 12.5 feet from the west end of the test cylinder and 2 feet upstream. It was set so that it determined the current at the level of the test cylinders. Signals from the current meter traveled through umbilicals to the Edgerton where they were monitored and recorded. In addition, a current meter traverse was performed using an Endeco current meter to determine the spatial differences in current along the test section. The current was found to be spatially uniform to within + or - 3.0% from end to end for all current speeds above 0.5 feet per second.

2.4 Tension Measuring System

The tension measuring and adjusting system was located at the east end of the experiment test section. Extensions were made to the two inner water jetted posts at this end. As shown in the diagram, a 5-foot extension was made to the center post and a 3-foot extension was made to the inner most post. What made this 3-foot extension different from the rest was that its attachment to the jetted pipe at the mudline was a pin connection as compared to the standard pipe couplings used on the other extensions. This pin connection gave it the ability to pivot in the plane of the posts. Onto this pivoting post, a hydraulic cylinder was mounted, horizontally, 2.5 feet above the mudline. The test cylinder was connected at one end to this hydraulic cylinder and at the other end to the drag measuring device. The test cylinder was attached 2.5 feet above the mudline, a sufficient distance to avoid any boundary layer effects

caused by the sandbar. A cable ran from the back of the hydraulic cylinder to a Sensotec Model RM In-Line load cell which was anchored at the other end to the center post. In this way, the force on the test cylinder was the same force seen by the load cell minus a small amount due to friction in the pin. The output from the tension load cell passed through the umbilicals to the Edgerton where it was monitored. Hydraulic hose ran from a hand operated pump on the Edgerton to the hydraulic cylinder so that the tension could be changed as desired. This was not a constant tension system. Stiction in the hydraulic cylinder kept the distance between the attachment points of the test cylinder a constant unless intentionally changed. Therefore tension varied slowly with current speed and mean drag force.

2.5 Test Cylinders

2.5.1 Cable

A 75 foot long instrumented cable was developed specifically for the experiments that were performed in the summer of 1981. The outer sheath for this cable was a single piece of clear flexible PVC tubing, which was 1 1/4 inches in outside diameter by 1.0 inch in inside diameter. Three 1/8 inch diameter stainless steel cables ran through the tubing and served as the tension carrying members. A cylindrical piece of 1/2 inch diameter neoprene rubber was used to keep the stainless steel cables spaced 120 degrees apart. The neoprene rubber spacer was continuous along the length except at seven positions where biaxial pairs of accelerometers were placed. Starting at the east end these positions were at L/8, L/6, L/4, 2L/5, L/2, 5L/8, and 3L/4. These accelerometers were used to measure the response of the cable. The accelerometers were Sundstrand Mini-Pal Model 2180 Servo Accelerometers which are sensitive to the direction of gravity. Each is 1/2 inch in diameter by 1.5 inches long. The biaxial pairing of these accelerometers made it possible to determine their orientation and hence extract real vertical and horizontal accelerations of the

cable at the seven locations. Three bundles of ten wires each ran along the sides of the neoprene spacer to provide power and signal connections to the accelerometers and to the drag measuring system. An Emerson and Cuming flexible epoxy was used to fill the voids in the cable and make it water tight. The weight per unit length of this composite cable was .7704 lbs/ft in air.

2.5.2 Steel Tubing

In a second set of experiments, the composite cable was placed inside a 1.631 inch O.D. by 1.493 inch I.D. steel tube. The tubing was made of four equal length sections that were joined together. At the internal joints steel nipples were welded to each tube section and stainless steel threaded couplings were used to join them. The tubing was connected to the hydraulic cylinder and to the drag cell mechanism by custom made universal joints to provide pinned end conditions. These special end connectors also kept the cable inside the tubing under a slight tension, and neoprene spacers at intervals of 18 inches between the cable and tubing inhibited any relative motion betwwen the two. The remaining cavity was allowed to fill with water. The weight per unit length of the steel tubing with the cable inside and the voids flooded with water was 2.2344 lbs/ft., in air.

2.5.3 Lumped Masses

In another set of experiments, lumped masses were fastened to the bare cable and their effects studied. The lumped masses were PVC cylinders 12.0 inches long and 3.5 inches in diameter. A 1.25 inch hole was drilled through the center of each lump so that the cable could pass through. In addition, four .625 inch holes were drilled symmetrically around this 1.25 inch center hole so that copper tubes filled with lead could be inserted to change the mass of the lumps. In the field, it was difficult to force the cable through the holes drilled in the PVC so each mass was cut in half along the length of its axis. The masses were placed on the cable in halves and held together by hose clamps. Different tests

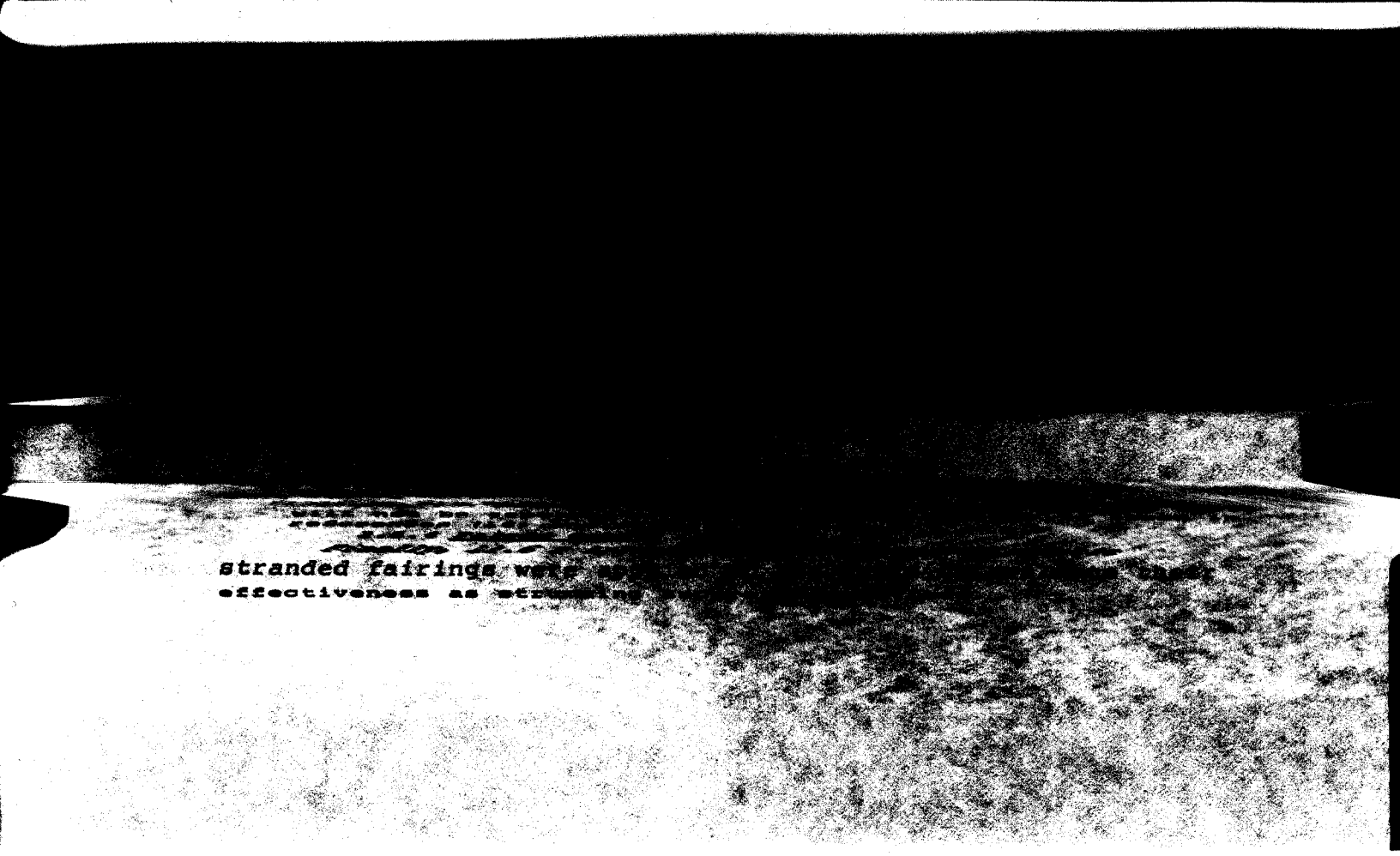
stranded fairings

were run by varying the number and location of lumps and by changing the mass of the lumps. The results of these tests will not be reported on in this paper, but may be found in references (16) and (17).

2.5.4 Faired Cable

Finally, 11.6 x 1/16 inch diameter Endeco plastic stranded fairings were applied to the cable to evaluate their effectiveness as strumming suppression devices.

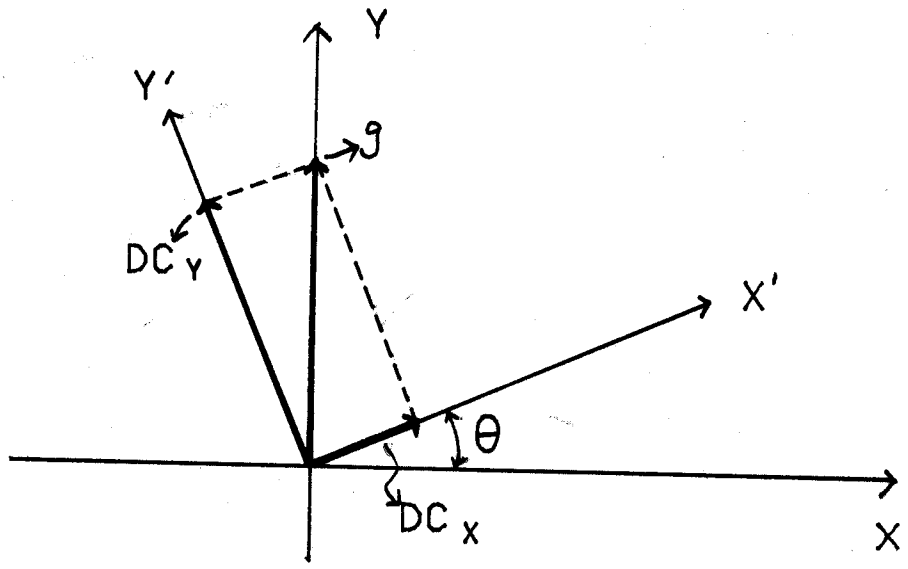

VECTOR ROTATION OF

RAW ACCELERATION

$$DC_X = \vartheta \sin \qquad \Rightarrow \quad \theta = \tan^{-1}\left(\frac{DC_X}{DC_Y}\right)$$

$$DC_Y = \vartheta \cos$$

$$X(t) = X'(t)\cos\theta - Y'(t)\sin\theta$$

$$Y(t) = X'(t)\sin\theta + Y'(t)\cos\theta$$

FIG. 3 RELATION BETWEEN ROTATED

ANGLE AND DC OFFSET

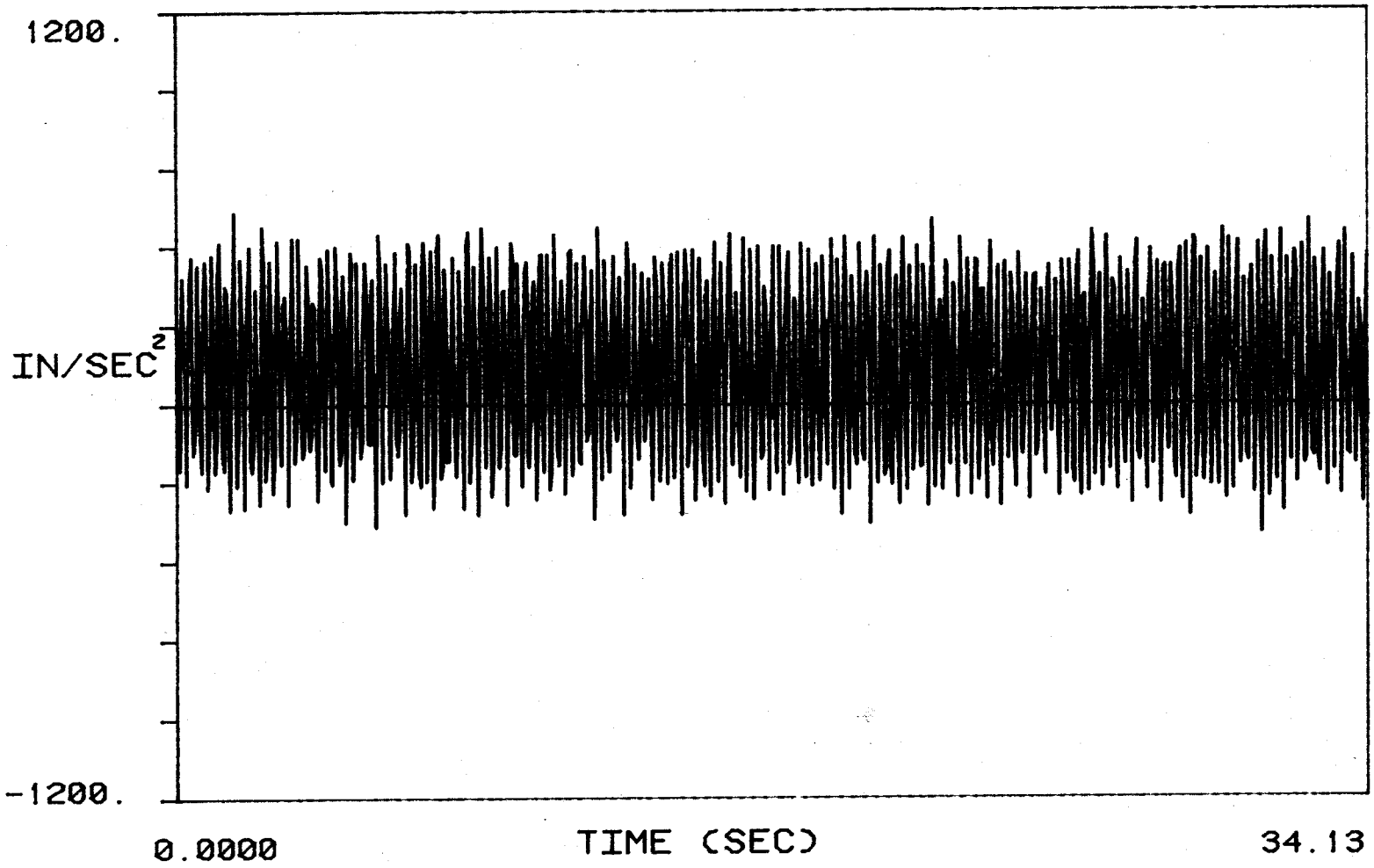

FIG. 4 RECORDED ACCELERATION BEFORE ROTATION NEAR HORIZONTAL

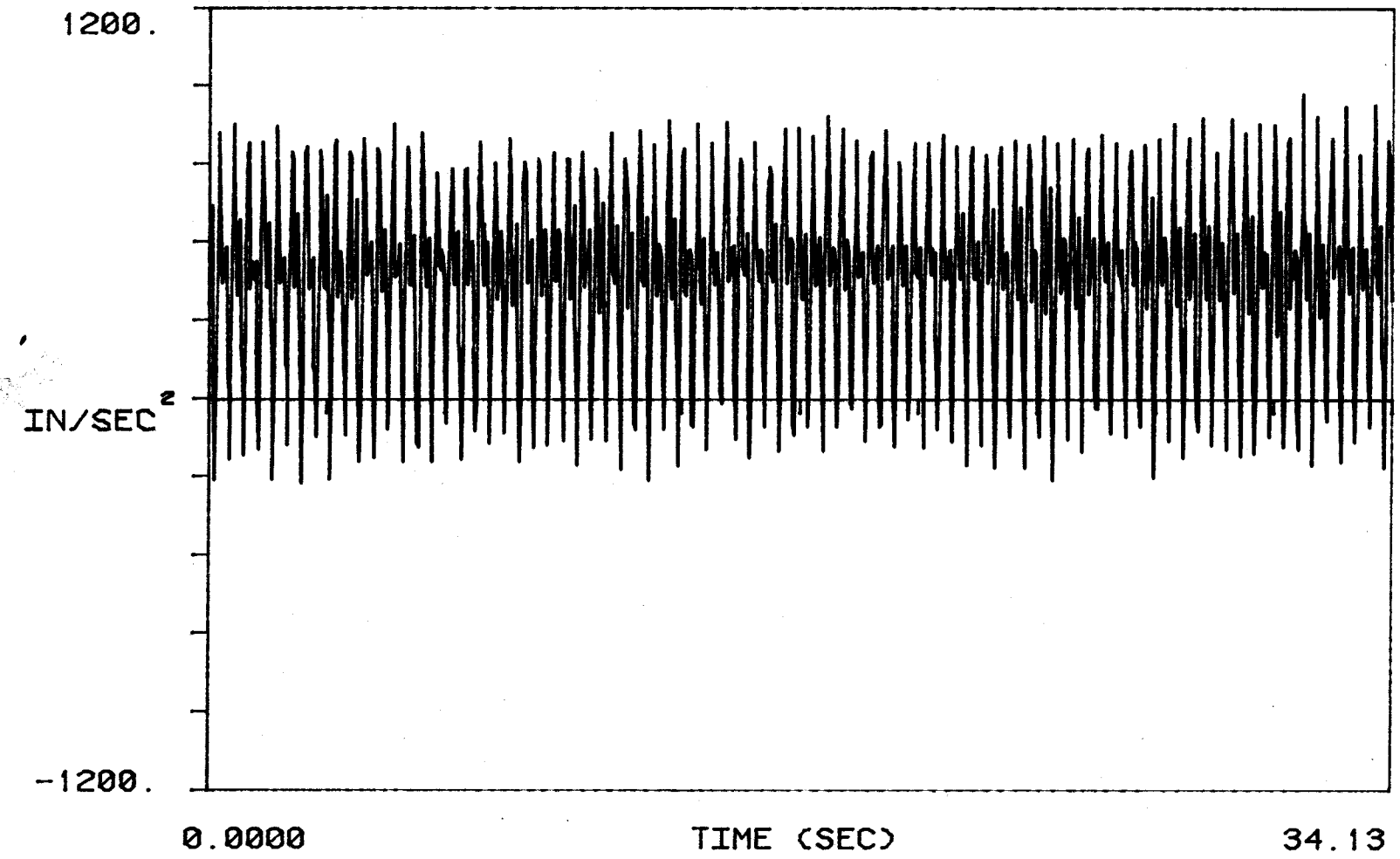

FIG. 5 RECORDED ACCELERATION BEFORE ROTATION NEAR VERTICAL,

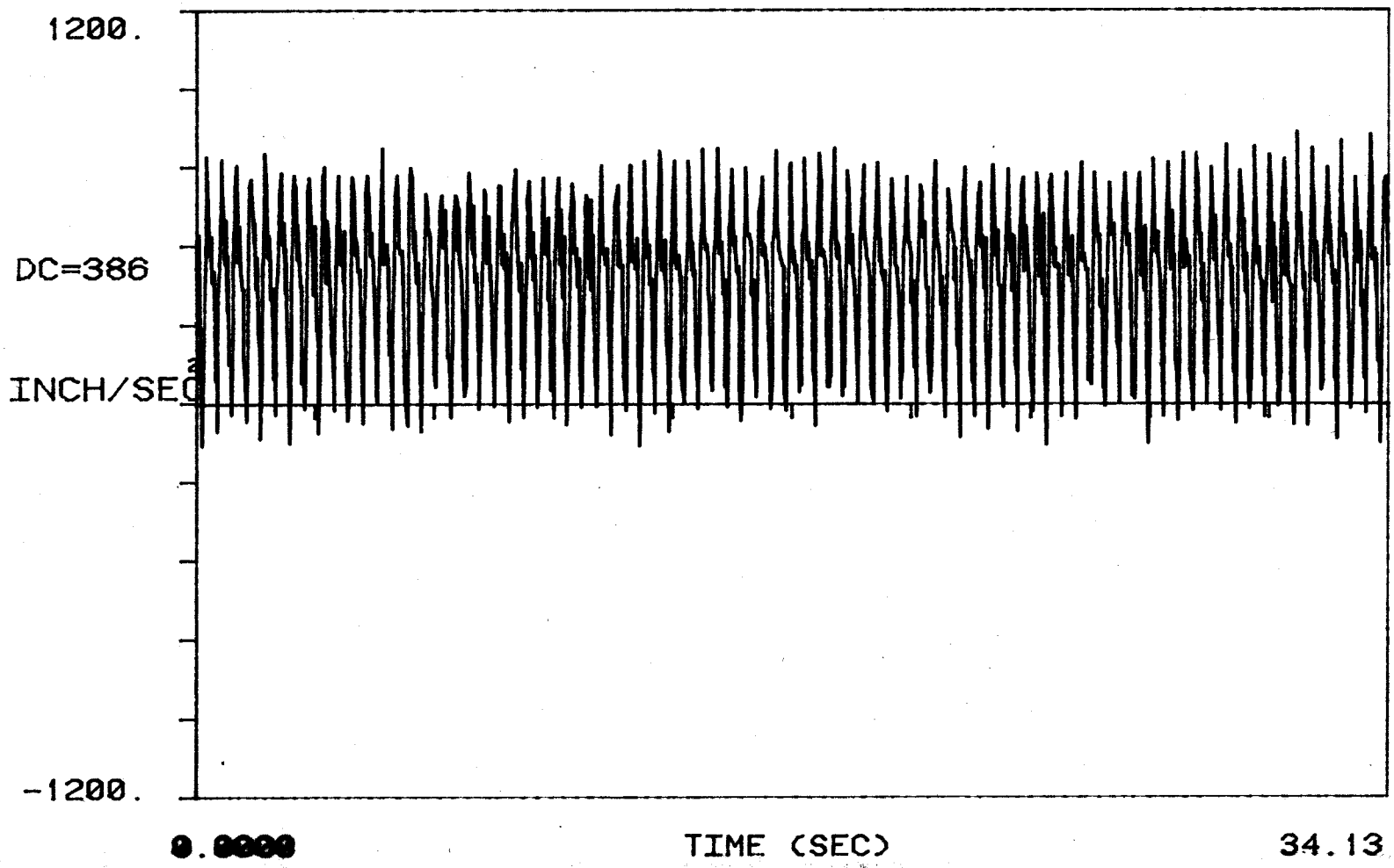

FIG. 6 REAL VERTICAL ACCELERATION

AFTER ROTATION OF 16.5 DEGREES

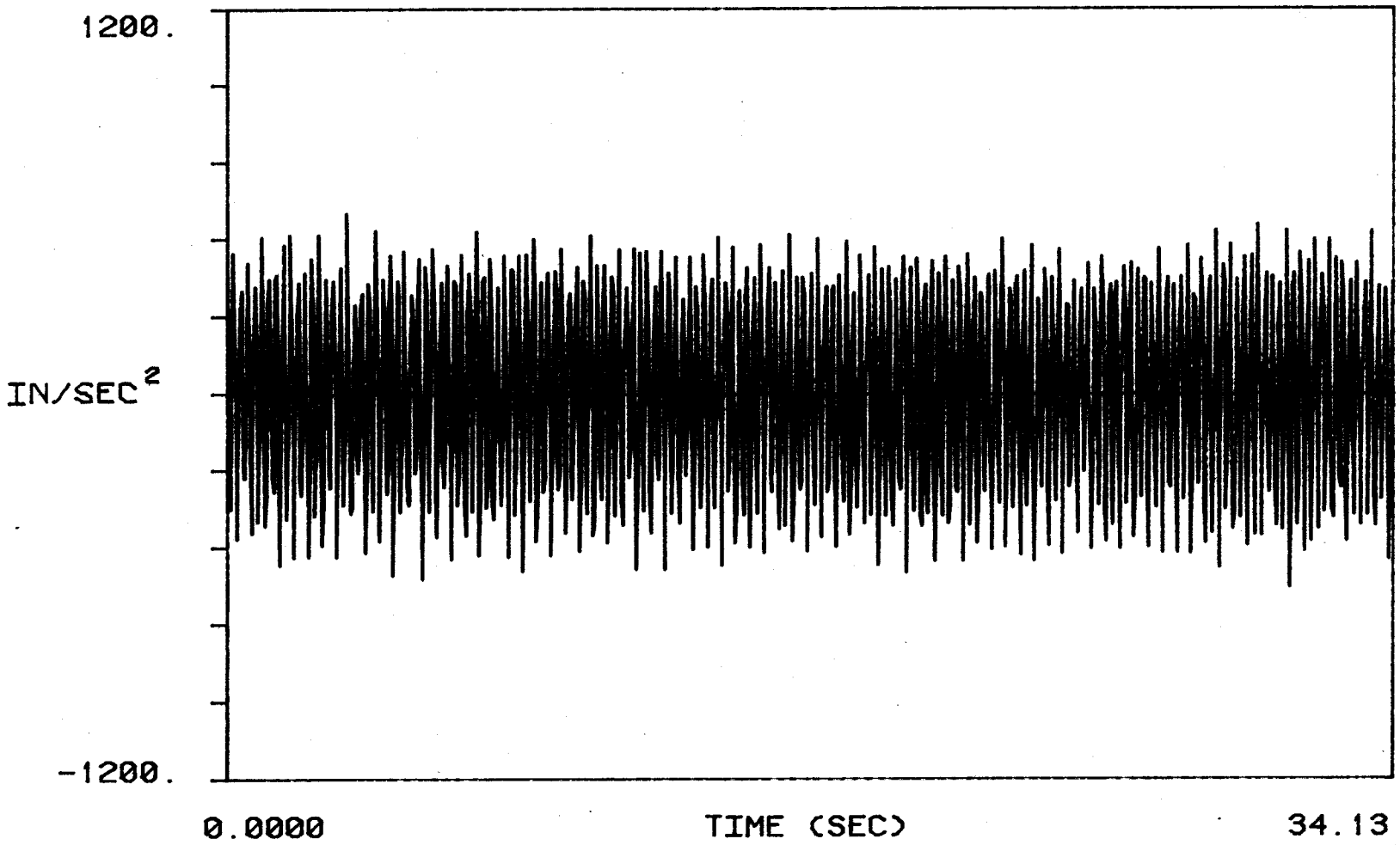

FIG. 7 REAL HORIZONTAL ACCELERATION
AFTER ROTATION OF 16.5 DEGREES

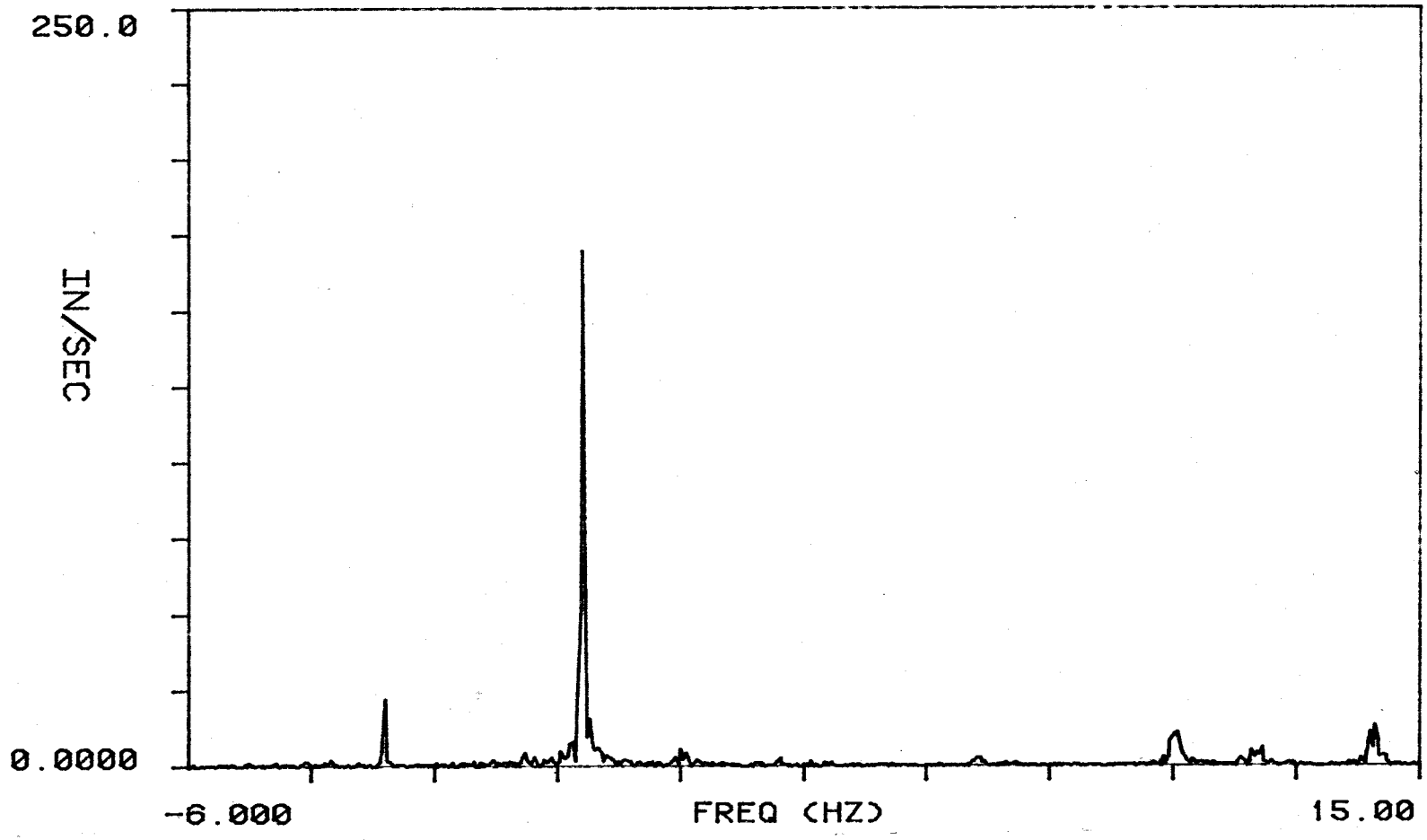

FIG.8 FFT OF THE ACCELERATION AFTER ROTATION

(HORIZONTAL RESPONSE)

$$V(t) = \int_0^t a(t')dt' \qquad (3.2.1)$$

A discrete time approximation for v(t) can be calculated by a linear constant coefficient difference equation.

$$V[n] = V[n-r]+T\sum_{k=0}^{m} b[k]a[n-k] \qquad (3.2.2)$$

where r is the order of the filter and the b(k) are the filter coefficients, m is the degree of the filter, and T is the sampling period.

Generally, the properties of digital integrators have been developed in the time domain by fitting the data points with a smoothed curve. The time domain interpretation as presented in equation 3.2.2 has an equivalent frequency domain formulation. The Z-Transform of equation (3.2.2) leads to the system function H(z):

$$H(Z) = T\,\frac{\sum_{k=0}^{m} b(k)z^{-k}}{1-z^{-r}} \qquad (3.2.3)$$

Evaluating H(z) on the unit circle of the z-plane yields the frequency response function H(w). If the numerator of H(z) is a mirror image polynomial then forward and backward integration in time will yield the same result. This leads to:

$$H(w) = Te^{-i(\frac{m-r}{2})w}\,\frac{\sum_{k=0}^{[m/2]} b(k)\cos(\frac{m}{2}-k)w}{i\sin rw/2} \quad \text{for m odd} \qquad (3.2.3a)$$

$$H(w) = Te^{-i(\frac{m-r}{2})w}\,\frac{\frac{1}{2}b(\frac{m}{2}) + \sum_{k=0}^{m/2-1} b(k)\cos(\frac{m}{2}-k)w}{i\sin rw/2} \quad \text{for m even} \qquad (3.2.3b)$$

The frequency response function for an ideal integrator is:

$$H_I(w) = \frac{T}{iw} \qquad (3.2.4)$$

Recognizing that, if x(n) and X(w) are a Fourier transform

pair, then x(n-m) and exp(-iwm)X(w) are also a Fourier transform pair. Any system function that can be written as:

$$H(iw) = |H(iw)|\ e^{ikw} \qquad (3.2.5)$$

where k is a constant, is a linear phase shift system. Let x(n) be the input to H(w) in equation 3.2.3 and Hi(w) in equation 3.2.4 with y(n) and y'(n) being the respective outputs. Rewriting H(w) and Hi(w) as:

$$H(iw) = |H(iw)|\ \frac{e^{-i\frac{m-r}{2}w}}{i} \qquad (3.2.6)$$

$$H_I(iw) = |H_I(iw)|\ \frac{1}{i} \qquad (3.2.7)$$

Then the transfer function between y(n) and y'(n) is,

$$\frac{Y(iw)}{Y'(iw)} = \frac{|H(iw)|}{|H_I(iw)|}\ \exp\left(-i\frac{m-r}{2}w\right) \qquad (3.2.8)$$

There is a linear phase shift between the ideal integrator result and this integrator result. A comparision of the magnitudes of (3.2.3) and (3.2.4) can be used to examine the accuracy of the integrator. An error measurement E(w) is defined as:

$$E(w) = 20 \log \frac{|H(w)|}{|H_I(w)|} = 20 \log w|H(w)| \qquad (3.2.9)$$

Fig. 9 shows E(w) for a variety of integrators. For the Castine experiment, the sampling frequency was 30 Hz, and the typical frequency range for the cable response was from 2 to 7 Hz. This corresponds to dimensionless frequencies in the figure from 0.13 π to 0.47 π where π corresponds to half the sampling frequency. Fig. 9 shows that the error for Trapezoidal rule integration in this range is from 2% to 20%, and 0.1% to 5% for Simpson's rule. The errors are larger at the higher frequencies. Many maximally flat integrators have been presented in the literature (6). Fig. 9 shows two examples for filters of degree m=2 and 4. The error for m=4

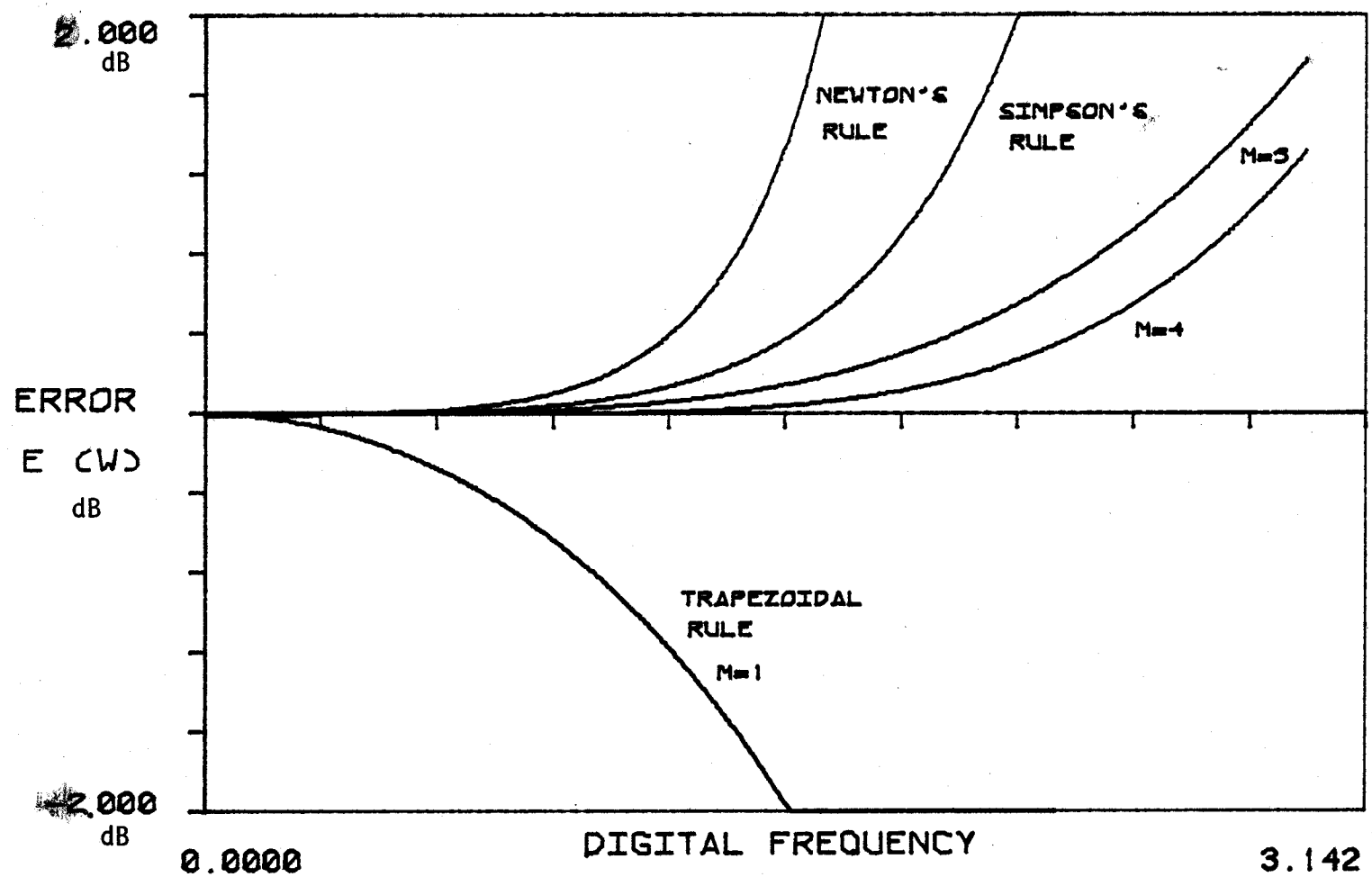

FIG.9 ATTENUATION FOR DIFFERENT INTEGRATORS

is reduced to a maximum of 0.5% at the highest frequency of interest.

Schuessler and Ibler (13) pointed out two basic mistakes in the application of this integration formula. First, the filter coefficients b(k) should be time-varying instead of constant according to the equation:

$$b'(k,n) = \begin{cases} b(k)\ u(n-r+k) & k=0,1,.,.,.,(r-1) \\ b(k) & k=r,r+1,.,.,m \end{cases} \qquad (3.2.10)$$

where b(k) are filter weights given in table 3.1 and 3.2 and u(k) is a unit step function. The reason is that according to the continuous integration equation (3.2.1) v(0)=0 must hold. But by using the digital integrator (3.2.2), v(0)=b(0)a(0) rather than zero. If (3.2.9) is used, v(0)=b'(0,0)a(0)=b(0)u(-r)a(0)=0 which yields the correct result. Second, the Newton-Codes formulas are, in fact, valid only for n=i*r with i=0,1.2 ..., so Schuessler and Ibler proposed that the sampling frequency at input and output should be different. This is accomplished by applying an interpolator to the input sequences before the integrator is applied. The combination of the interpolator and integrator into one system led them to propose a new integration formula.

$$V(n) = V(n-1) + \frac{T}{3} \sum_{k=0}^{2L-1} b'(k,n)\ a(n-k) \qquad (3.2.11)$$

where L is the length of the interpolator and

$$b'(n,k) = \begin{cases} b(k)\ u(n-L+k) & 0 \le k \le L-1 \\ b(k) & L \le k \le 2L-1 \end{cases} \qquad (3.2.12)$$

the b(k) are the new filter coefficients given in table 3.3 This integrator was used in the analysis of the Castine data.

3.3 Low Frequency Noise Expansion

The cable velocity, v(t), and displacement, d(t), can be obtained from the acceleration, a(t), by numerical

integration. If v(0) is the initial velocity at t=0, the time of the start of data collection, then

$$v(t) = v(0) + \int_0^t a(t')dt' \qquad (3.3.1)$$

The initial velocity v(0) is unknown. However, a bounded displacement d(t) is desired. This requires that there be no linear trend or DC component in the velocity v(t). The value v(0) can be arbitrarily set to zero. Following the integration of a(t) a atraight line is fitted to v(t). The offset and trends which are found may be then removed from v(t). Equation 3.3.1 can be rewritten as:

$$v(t) = a(t) * u(t) \qquad (3.3.2)$$

where u(t) is the unit step function and * denotes a convolution integral. Taking the Fourier transform of Equation 3.3.2 yields:

$$V(w) = A(w)[\pi\delta(w) + \frac{1}{iw}] = A(0)\pi + \frac{A(w)}{iw} \qquad (3.3.3)$$

$$A(0) = \int_{-\infty}^{\infty} a(t)dt \qquad (3.3.4)$$

The term A(0) can be removed by fitting a straight line to a(t) to remove any linear trend or DC component in acceleration a(t). The transfer function between a(t) and v(t) is:

$$H(w) = \frac{V(w)}{A(w)} = \frac{1}{iw} \qquad (3.3.5)$$

The same procedure can be applied to integrate v(t) to get d(t) except that the assumption for the zero mean d(t) is no longer true. But, we are interested only in the dynamic response of the cable, so d(0) can be set arbitrarily. Integration has the characteristics of a low-pass filter with a gain which goes to infinity as the frequency goes to zero. This leads to the undesirable expansion of low frequency noise in the integration process. Fig. 7 shows a sample of

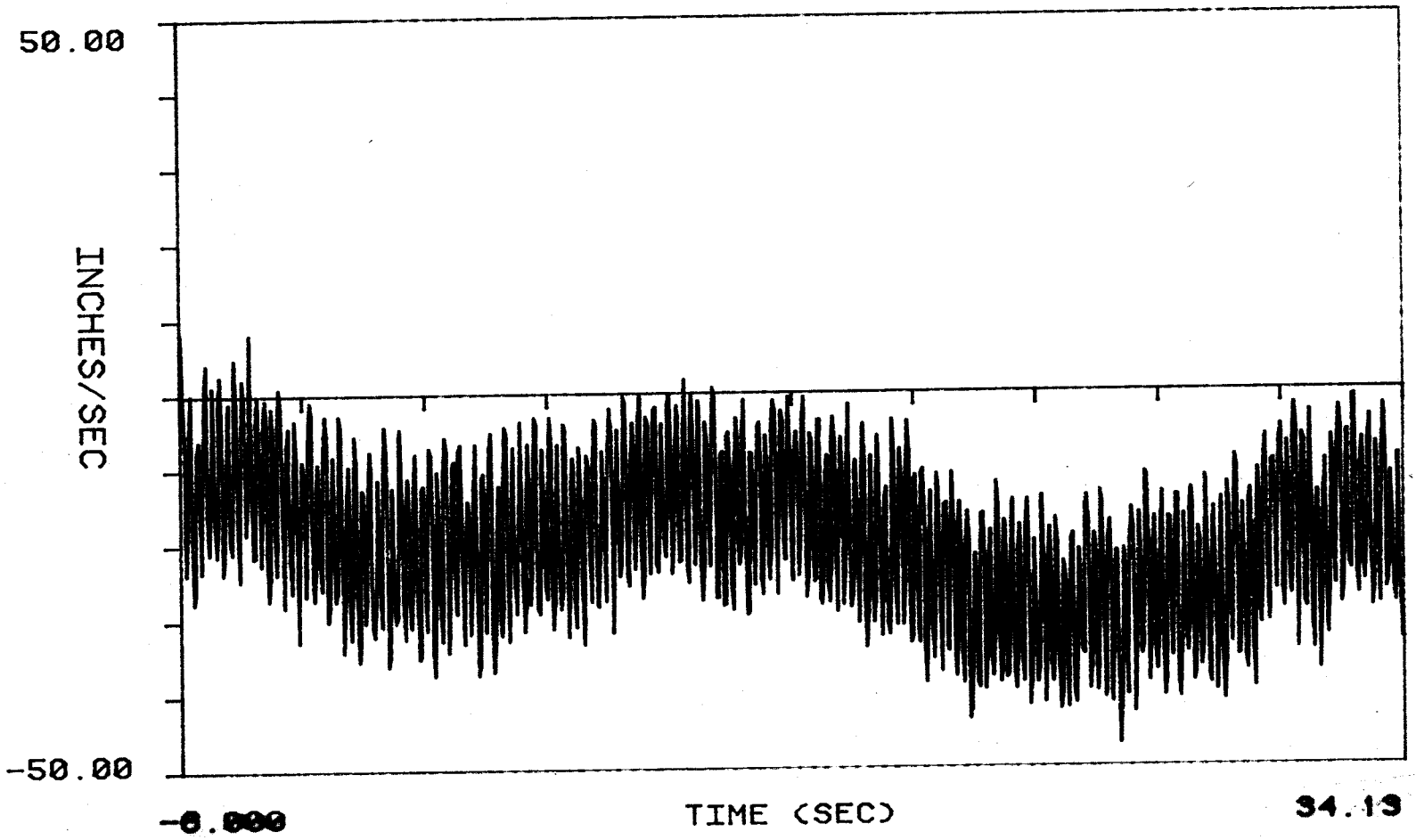

FIG. 10 VELOCITY AFTER ONE INTEGRATION WITH LOW-FREQUENCY NOISE EXPANSION

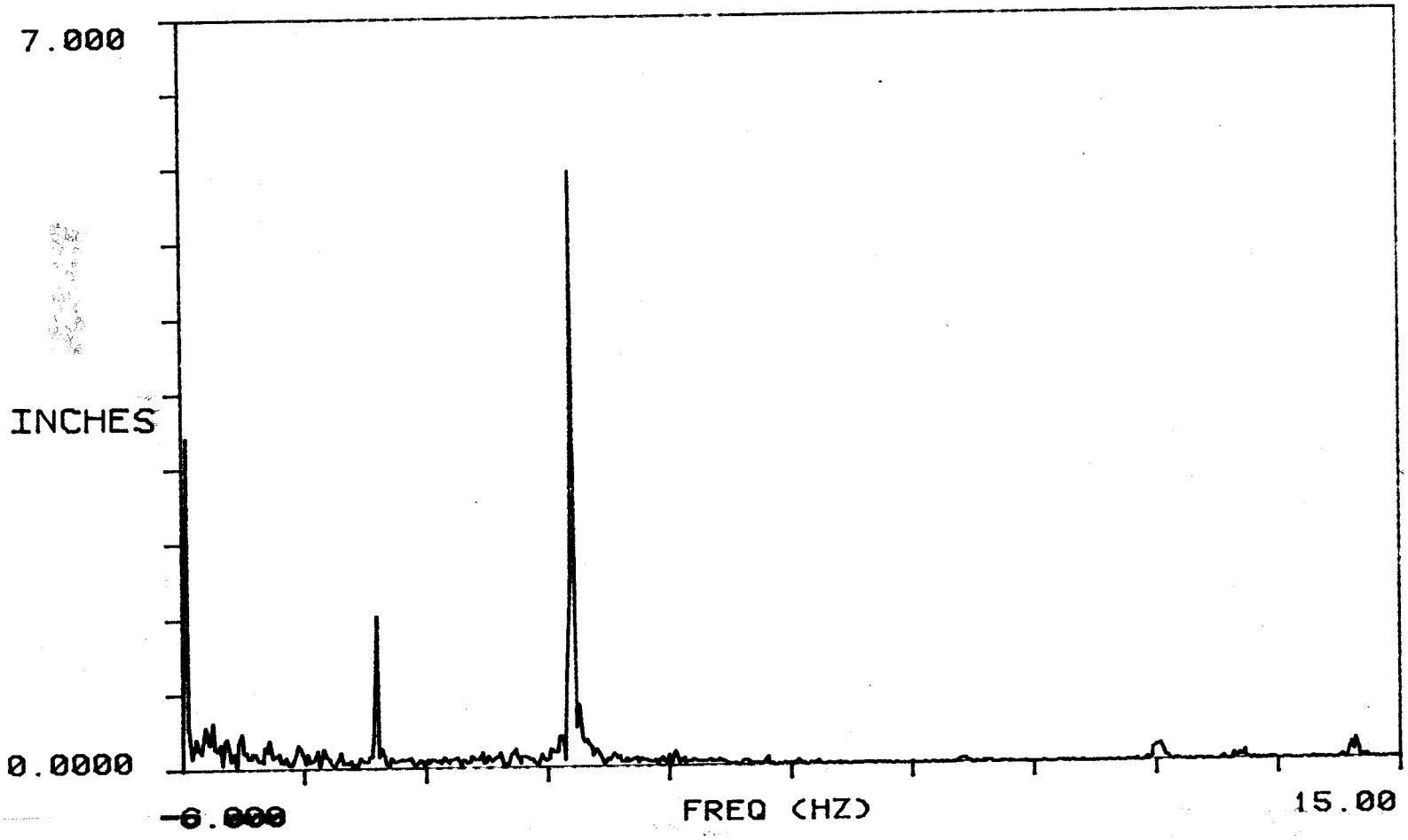

FIG.11 FFT OF THE VELOCITY IN FIG.10

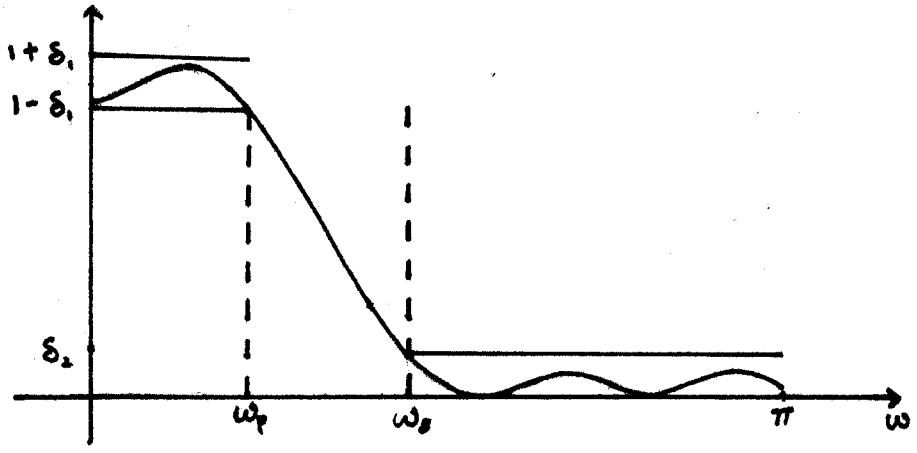

FIG. 12 FILTER SPECIFICATION

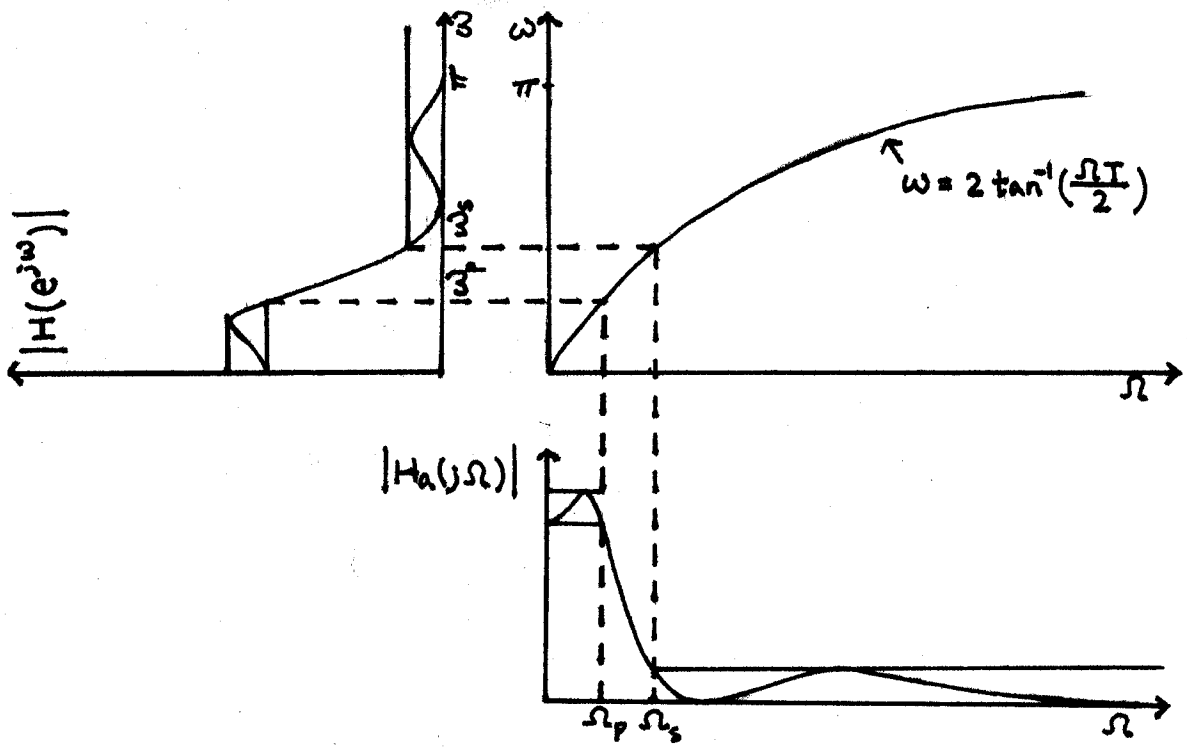

FIG. 13 ANALOG-DIGITAL BILINEAR TRANSFORMATION

an acceleration time history. Fig. 8 is the FFT of this acceleration. A negligible component of low frequency noise is shown. Figures 10 and 11 show that after integration, low frequency noise dominates the velocity signal.

This reveals that low frequency noise expansion leads to unacceptable integration errors. To correct the problem, a high-pass filter is required.

3.4 High-Pass Filter

A digital filter is a linear time-shift-invariant system represented by a linear constant coefficient difference equation (LCCDE):

$$y[n] = \sum_{k=1}^{N} a_k\, y[n-k] + \sum_{k=0}^{M} b_k\, x[n-k] \qquad (3.4.1)$$

The corresponding system function is given by

$$H(Z) = \frac{\sum_{k=0}^{M} b_k\, Z^{-k}}{1 - \sum_{k=1}^{N} a_k Z^{-k}} \qquad (3.4.2)$$

where x(n) is the input signal, y(n) is the output signal, and ak and bk are filter coefficients. For a stable causal filter all the poles of this system function must lie inside the unit circle. There are three basic steps in the design of a digital filter: (1) The specification of the desired filter properties; (2) the determination of the transfer function possessing those properties and (3) the implementation of the filter.

For an ideal low-pass (or high-pass) filter, the transfer function magnitude contains a sharp discontinuity at the cut-off frequencies and the required filter order is infinite. Thus a transition band at the cut-off frequencies and a tolerance error in pass-band and stop-band are provided to approximate the desired filter. In step (1), the filter specification must include these tolerance magnitudes and the transition bandwidth. Fig. 12 shows these specifications for a low-pass filter.

If the system function H(z) in (3.4.2) contains poles

solely at the origin, the filter is called a finite impulse response (FIR) filter. Otherwise it is an infinite impulse response (IIR) filter.

A FIR filter is always stable and a linear phase is always achievable by choosing a symmetric impulse response function h(n). For the same desired filter characteristics, the FIR filter must be of a much higher order than the comparable IIR filter, and therefore the FIR filter may require excessive computer time.

The design of an IIR filter involves the transformation of an analog filter into a digital filter. There are several analog low-pass filters available, including the Butterworth, Chebyshev, and elliptic filters. By using the proper transformation between the analog and digital systems, an analog low-pass filter can be designed for which the corresponding digital filter meets the desired specification.

There are two requirements for the transformation of an analog system into a digital system. First, the imaginary axis of the s-plane must map onto the unit circle of the z-plane. This means that the properties of the frequency response function have been preserved. The second requirement is that a stable analog filter must be transformed into a stable digital filter, i.e. all the poles in the left half s-plane must map into the inside of the unit circle in the z-plane.

The Bilinear transformation (10) for mapping between the s-plane and the z-plane is given as:

$$S = \frac{2}{T}\,\frac{1-z^{-1}}{1+z^{+1}} \qquad (3.4.3)$$

The unit circle in the z-plane is mapped according to:

$$S = \frac{2}{T}\,\frac{1-e^{-jw}}{1+e^{-jw}} = \frac{2}{T}\tan\frac{w}{2} = \sigma+i\Omega \rightarrow \Omega = \frac{2}{T}\tan\frac{w}{2} \qquad (3.4.4)$$

Thus, the unit circle is mapped onto the imaginary axis of

the s-plane. Also, the left half of the s-plane is mapped into the inside of the unit circle of the z-plane. Fig. 13 demonstrates the transformation. The procedure to design an IIR low-pass filter involves the following four steps:

(1): Specifying the desired filter properties.

(2): Mapping those specifications into an analog filter using the Bilinear transformation.

(3): Choosing an analog filter and determining those parameters which meet the analog filter specification requirements.

(4): Mapping the analog filter to a digital filter using the bilinear transformation.

A high-pass filter can be designed by applying an appropriate frequency transformation from a low-pass filter. Let H(zl) and H(z) be the desired system functions of the high-pass filter and corresponding low-pass filter. One method of transformation is by using the following relation:

$$z^{-1} = - \frac{\alpha + z_1^{-1}}{1 + \alpha z_1^{-1}} \qquad (3.4.5)$$

Fig. 14 shows the relation between H(wl) and H(w). The design procedure for a high-pass filter involves the following steps:

(1): Specification of the desired high-pass filter H(wl)

(2): Transformation to the equivalent low-pass filter H(w) using equation (3.4.5)

(3): Application of the steps for the design of a low-pass filter H(w)

(4): Transformation to the high-pass filter H(wl) by using equation (3.4.5)

An IIR elliptic high-pass filter of the smallest possible order is used to prevent low frequency noise expansion in the double integration procedure. A computer program for the design of an IIR elliptic filter has been published by Gray and Markel (5). The input data to this program includes the tolerance error in pass-band and

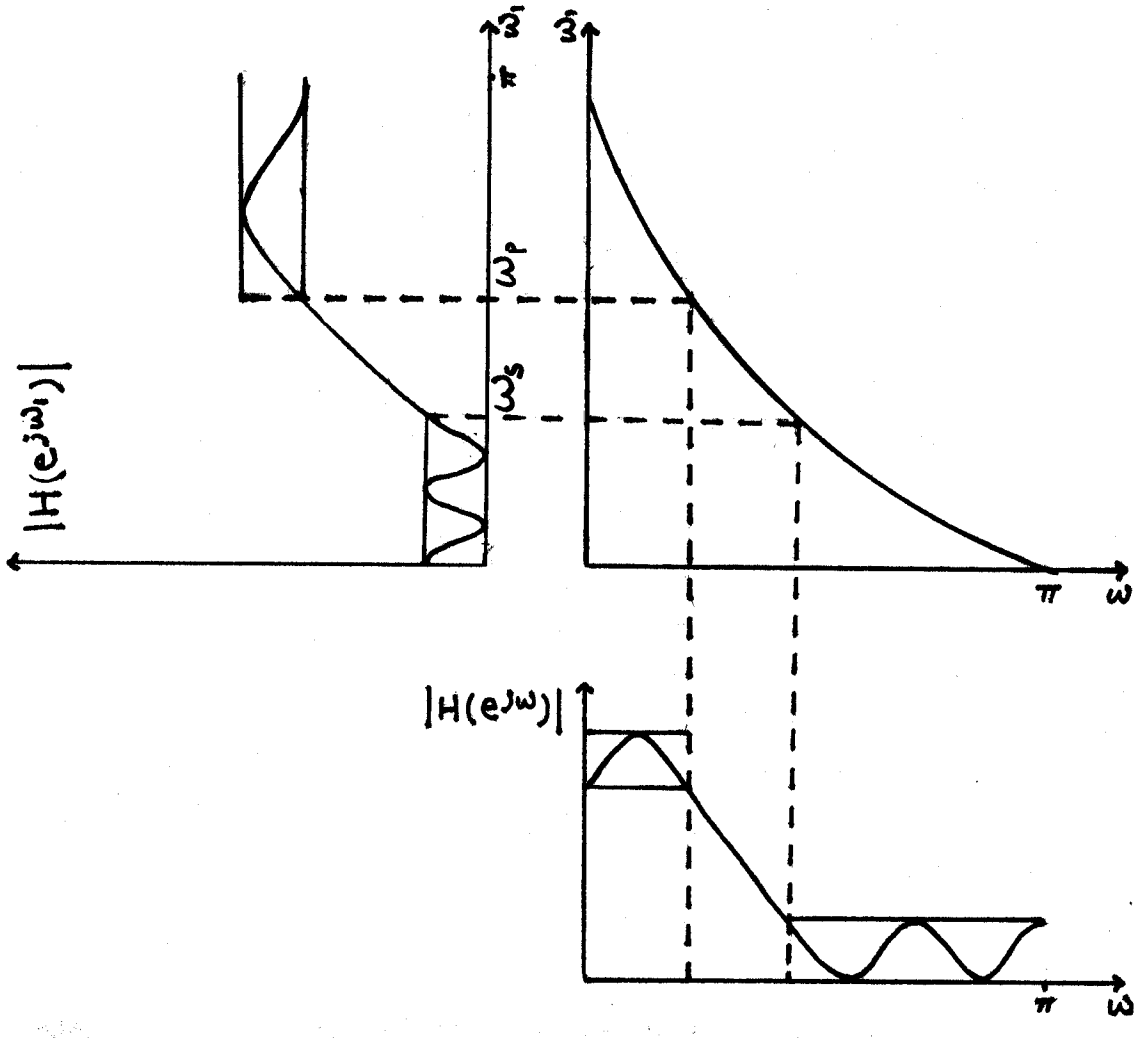

FIG. 14 TRANSFORMATION FROM LOW-PASS TO HIGH-PASS

stop-band, the stop-band and pass-band edge frequencies and the filter order N which may be estimated from design charts (10). The output gives the position of zeros and poles for the desired filter system function H(z).

A cascade form of implementation is used by writing H(z) as a product of second-order factors as:

$$H(Z) = \prod_{k=1}^{N/2} (a_{0k} + a_{1k}Z^{-1} + a_{2k}Z-2) \qquad (3.4.6)$$

This separates the whole system into a series of several second-order systems. The output of one system becomes the input of the next. In general, this form of implementation is less sensitive to the parameter quantization effect.

An IIR recursive filter always has nonlinear phase characteristics. For this research, accurate phase information is required in order to conduct the modal analysis. The following steps (11) were used to eliminate the nonlinear phase effects. Let x(n) and y(n) be the sequences before and after the filter respectively. R is the time reverse device, and H(z) is the filter system function. These can be used in the following sequence

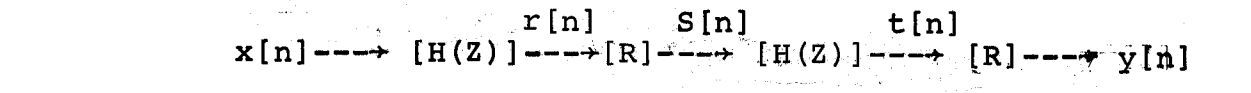

$$R(w) = X(w)\ H(w)$$
$$S(w) = R(-w)$$
$$T(w) = S(w)\ H(w)$$
$$Y(w) = T(-w) \qquad (3.4.7)$$

Those relations imply the following:

$$Y(w) = X(w)H(w)H(-w) = X(w)\,|H(w)|^2 \qquad (3.4.8)$$

The new system function between x(n) and y(n) is the square of the magnitude of the original filter's system function and has zero phase shift.

3.5 Double Integration Procedures

A summary of the procedure for double integrating a digital acceleration signal follows. The procedure contains

the following eleven steps:

Step 1. Determine the rotation angle of the accelerometers and use them to obtain the real vertical and horizontal accelerations.

Step 2. Using the method of least squares, fit a straight line to the block of data to be integrated. Use this to remove DC offsets and trends from the data prior to integration. The block length is 1024 data points in the results presented here.

Step 3. Obtain the acceleration spectrum and divide it by 1/w**4 to obtain the theoretical displacement spectrum. Use these two spectra as a subjective aid in the determination of the high-pass cutoff frequency necessary for the prevention of low-frequency noise expansion.

Step 4. High-pass filter the acceleration signal using an IIR elliptic filter to remove any low frequency noise.

Step 5. Integrate the acceleration signal using the Schuessler-Ibler integrator to obtain velocity.

Step 6. Least square fit a straight line to the velocity time history to remove the DC offset and linear trend.

Step 7. High-pass filter the velocity signal using the IIR elliptic filter to remove low-frequency components that were expanded in Step 5.

Step 8. Integrate the velocity signal using the Schuessler-Ibler integrator to obtain displacement.

Step 9. Least squares fit a straight line to the displacement time history to remove offsets and linear trend.

Step 10. High-pass filter the displacement signal using the IIR elliptic filter to remove low-frequency components that were expanded in Step 8.

Step 11. Plot summary data such as root-mean-squares, spectra, time series and two dimensional cylinder

motion time series.

CHAPTER 4
RESPONSE OF CYLINDERS

In the preceeding chapter, the data analysis process was presented, including vector rotation, filter design, and double integration procedures. In this chapter, typical analysis results of cylinder motions at lock-in and non-lock-in are presented. Compressed 2 1/2-hour records of drag coefficient, current speed, and RMS displacement response are also presented.

4.1 Cylinder Motion at Lock-in

Lock-in occurs when the vortex shedding frequency falls within a few percent of a natural frequency of the cylinder. The vortex shedding process is synchronized with the cylinder's motion, and a stable sinuisoidal transverse displacememt of nearly constant amplitude is observed. Fig. 15 shows an example of cross flow displacement of the pipe at L/4 during lock-in with the third mode. Fig. 16 is the corresponding FFT. A single dominant peak is observed. A narrow-band lift force is associated with this response.

In the horizontal direction, the motion is quite different from the vertical response at lock-in. A periodic but nonsinusoidal displacement is observed in the horizontal direction as shown in Fig. 17. Fig. 18 presents the magnitude of the FFT. The dominant frequency in horizontal direction is exactly double that in the vertical direction. The reason for this is that during the shedding of two vortices, one from each side off the cylinder, the lift force completes one cycle, but in the horizontal direction the drag force variation completes two cycles, one for each vortex shed. The result is that the dominant horizontal response frequency is exactly twice that of the vertical. The FFT in Fig. 18 reveals that the horizontal vibration also includes a small response component at the cross-flow vibration response frequency. This secondary frequency component accounts for the beat phenomena in Fig. 17. At lock-in the vertical and

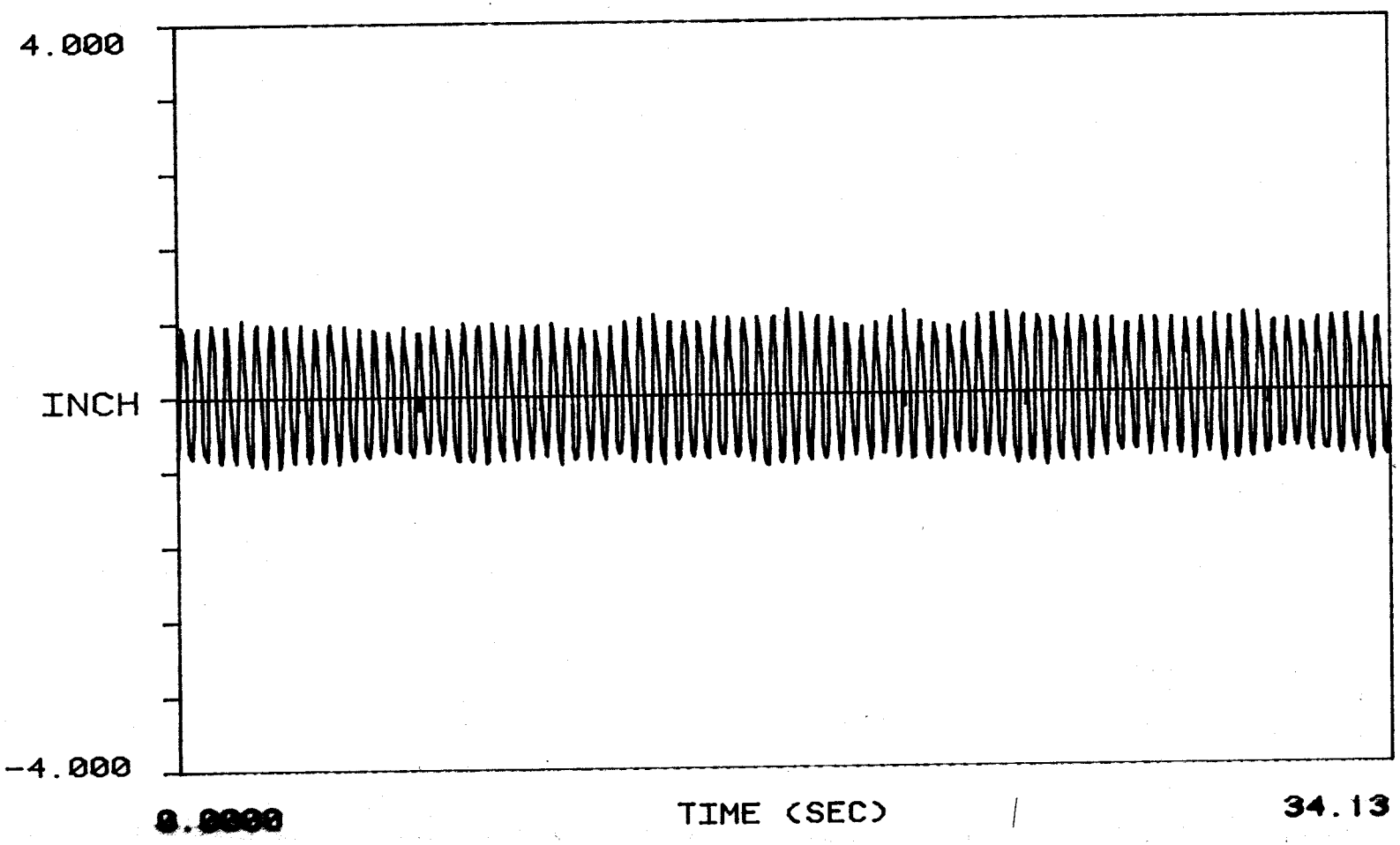

FIG.15 VERTICAL DISPLACEMENT OF
THE PIPE AT LOCK-IN AT L/4

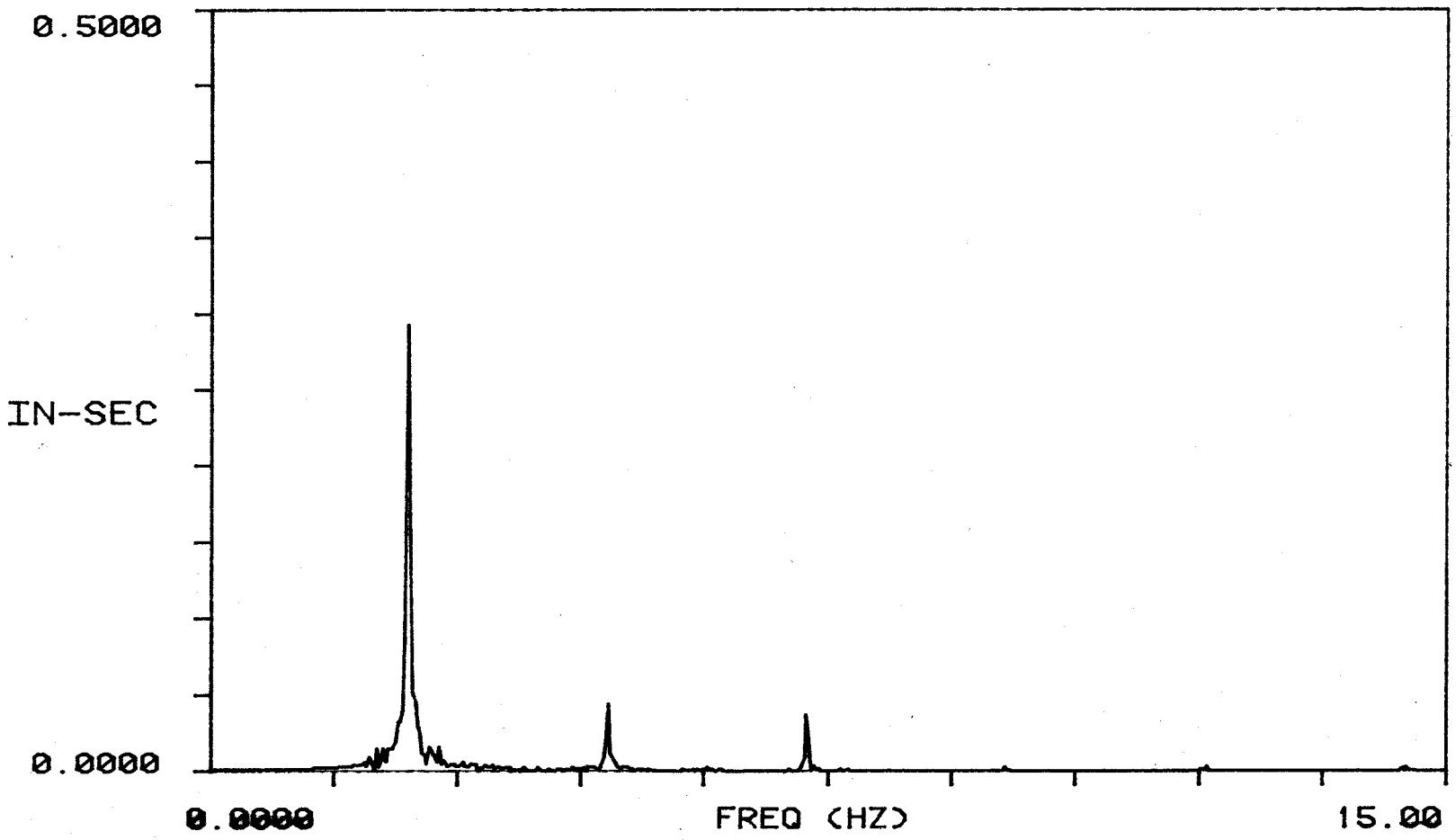

FIG.16 FFT OF THE DISPLACEMENT IN FIG.15

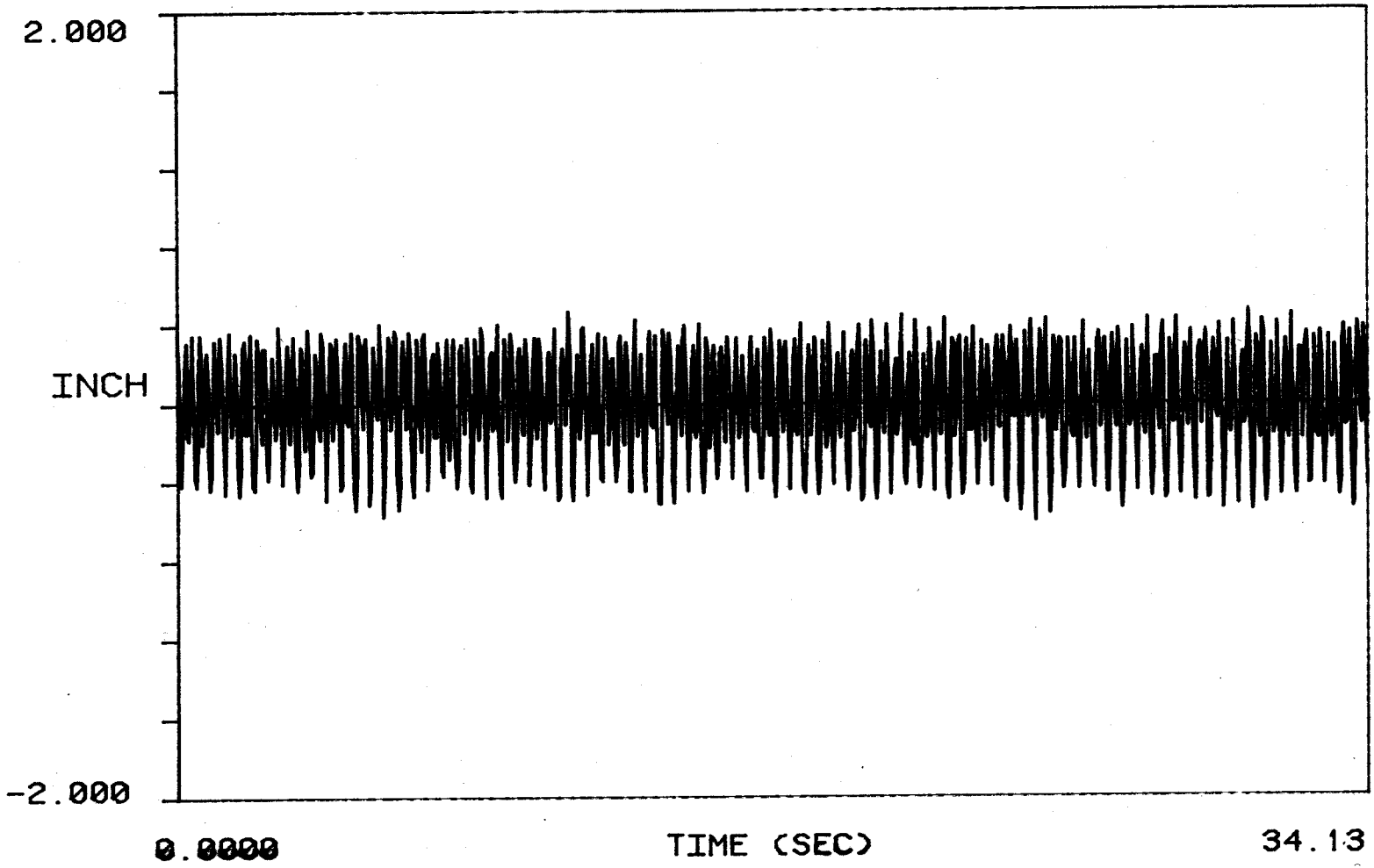

FIG.17 HORIZONTAL DISPLACEMENT OF THE PIPE AT LOCK-IN AT L/4

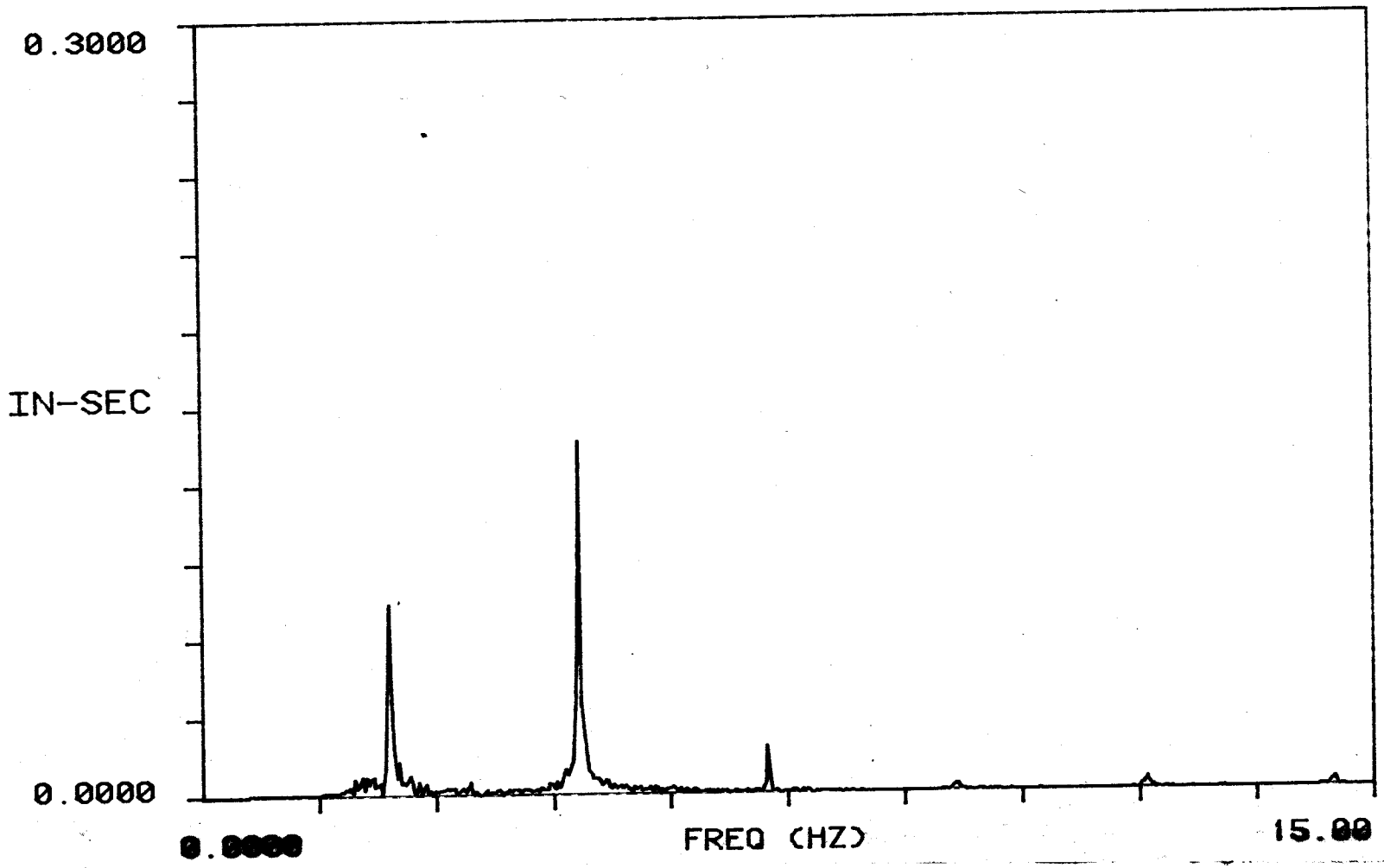

FIG.18 FFT OF THE DISPLACEMENT IN FIG.17

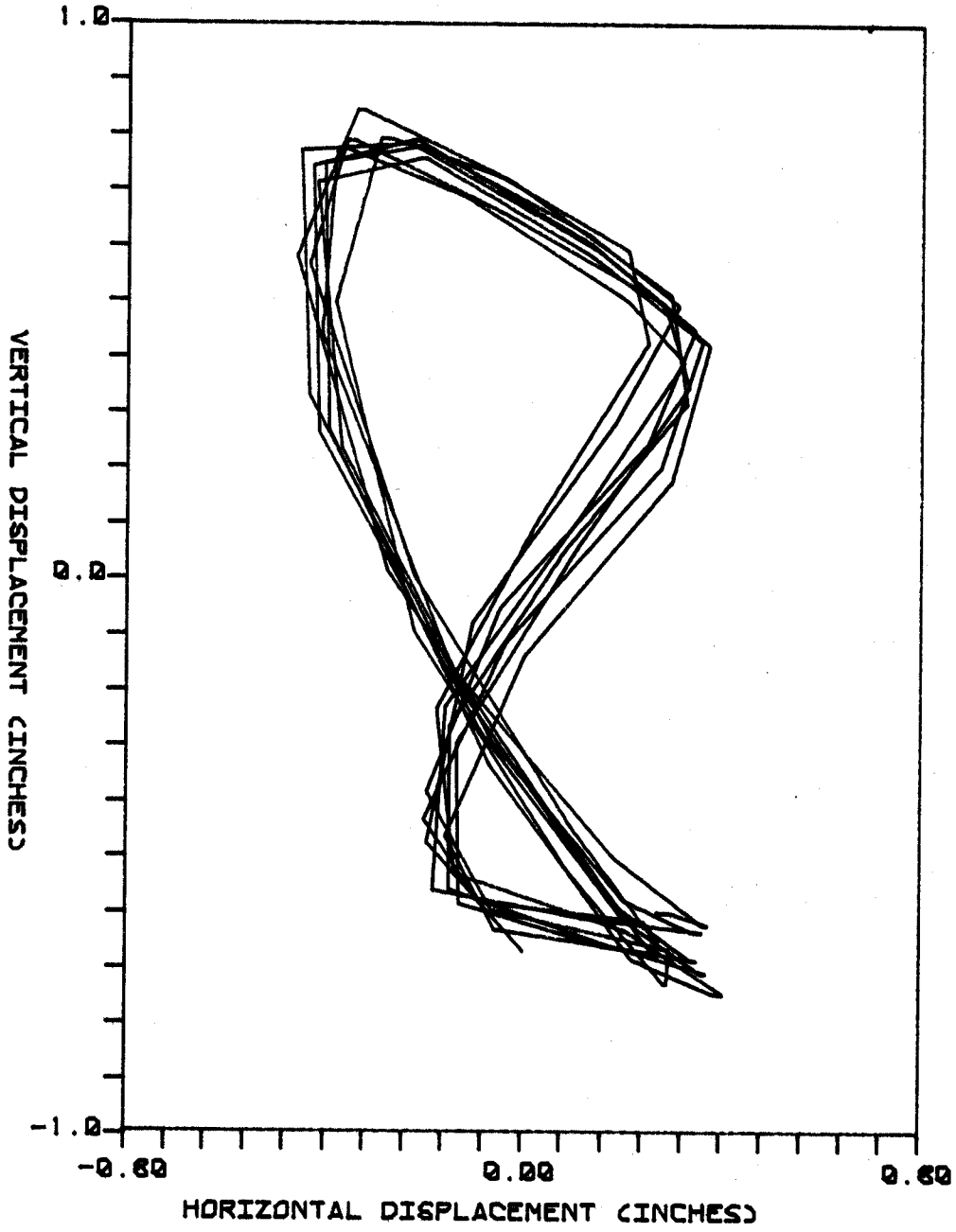

FIG. 19 TWO-DIMENSIONAL MOTION TIME HISTORY AT LOCK-IN AT L/4

horizontal excitations and responses are highly correlated. By double integration of both horizontal and vertical accelerations to obtain displacement time histories, it is possible to plot the trajectary of the motion of a point on the cylinder. Fig. 19 shows the motion at L/4 projected on to a plane which is normal to the cylinder axis. In this case the vertical motion was lock-in at third-mode and the horizontal motion was at twice the frequency of the vertical motion and was dominated by response in the fifth-mode. A small amount of third-mode motion also appears in the horizontal response. Without it there would be nearly perfect figures of eight.

At this point in the analysis, one does not generally know for certain which natural modes of vibration are responding. It will in fact be shown that the horizontal response which results from cross-flow lock-in does not always excite a resonant natural frequency. Mode shape identification is required to isolate individual contributing vibration modes. This is discussed in Chapter 5.

4.2 Cylinder Motion at Non-lock-in

When the vortex shedding frequency is outside of the lock-in range, non-lock-in vibration results. The response is characterized by fluctuations of amplitude and frequency in both vertical and horizontal directions. The lift force correlation length along the cylinder becomes much shorter than that at lock-in. Figs. 20 through 23 show typical displacement time histories and their FFTs in the cross-flow and in-line directions at L/8. Wide band lift and drag forces are implied. Figure 24 shows the corresponding displacement trajectories at L/8. For the data presented in Figs. 20 and 22, the response is due to many different modes. As will be shown in Chapter 5, the horizontal response peaks in Fig. 23 are due to the fourth, fifth, sixth and seventh modes.

4.3 Current, Drag Coefficient and RMS Displacement

The RMS data for in-line and transverse displacements

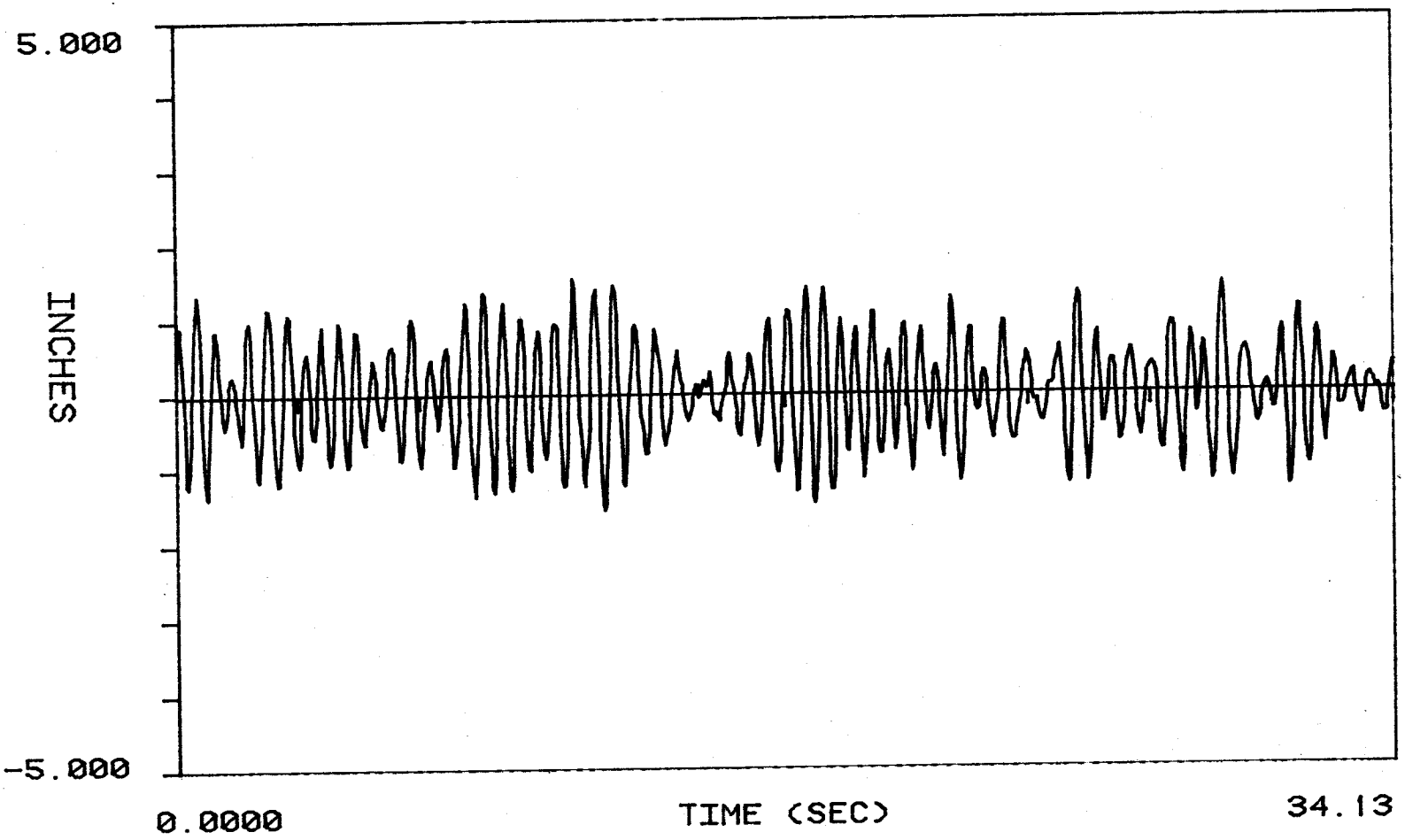

FIG.20 VERTICAL DISPLACEMENT OF
THE PIPE AT NON-LOCK-IN AT L/8

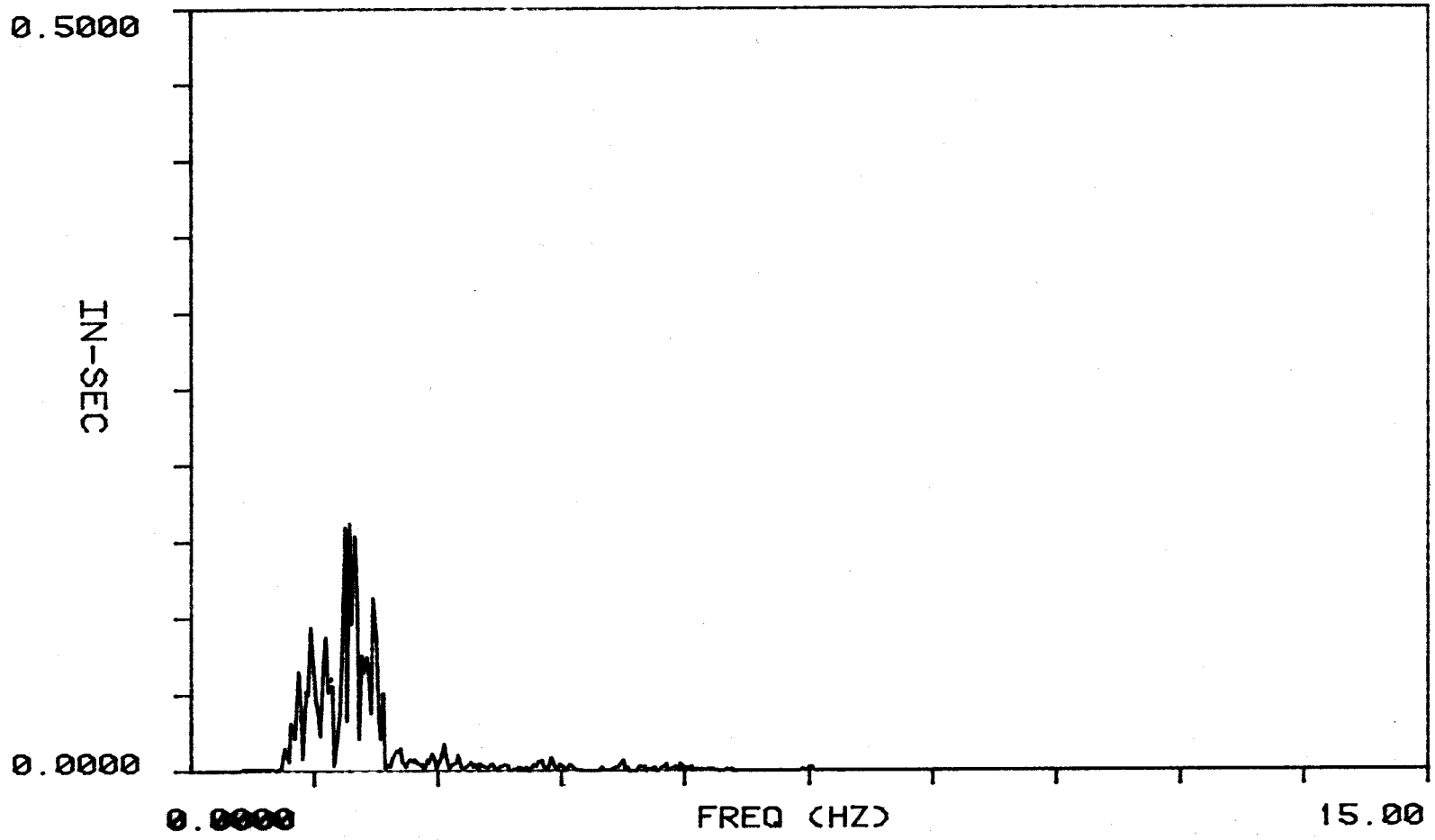

FIG.21 FFT OF THE VERTICAL DISPLACEMENT IN FIG.20

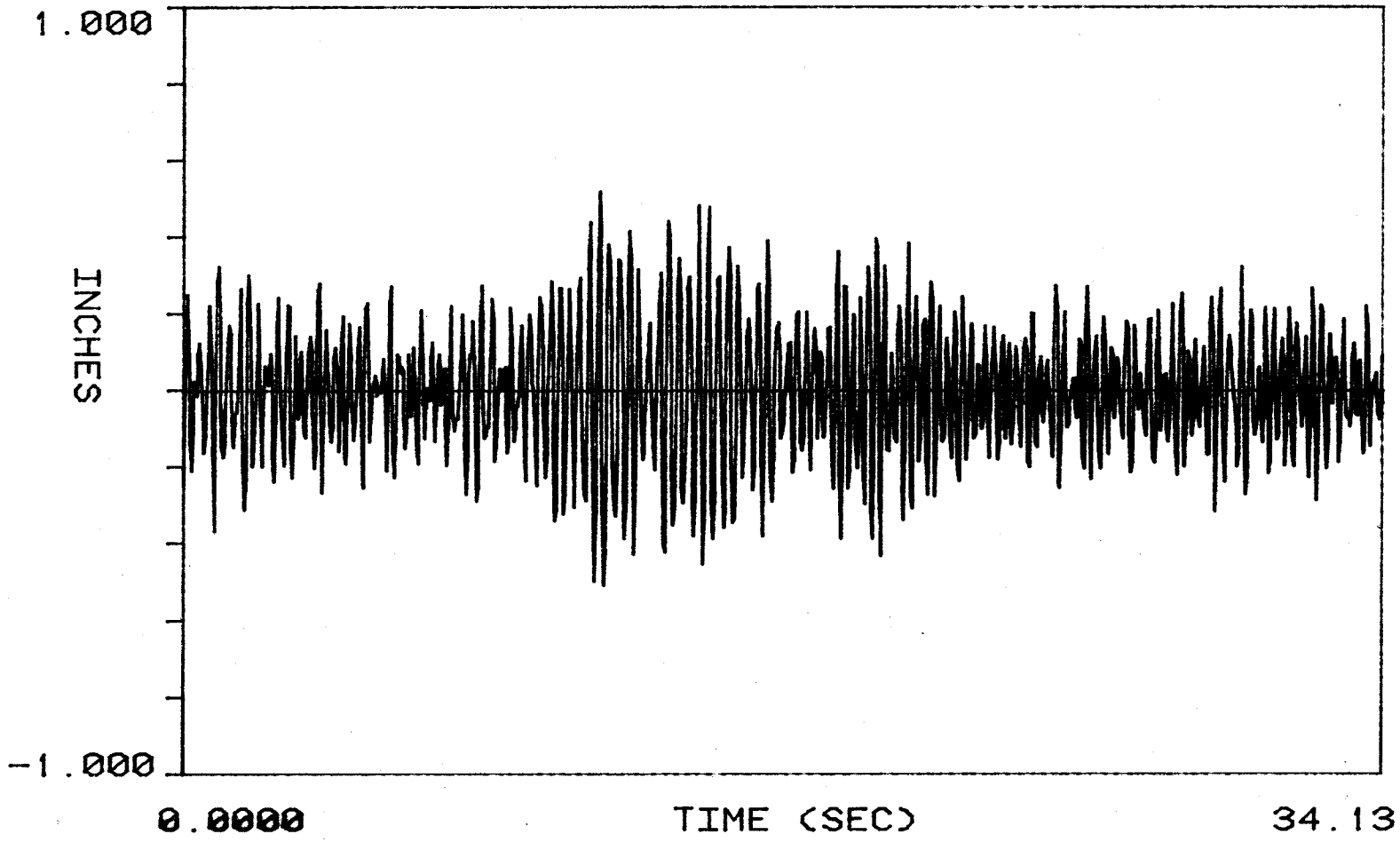

FIG.22 HORIZONTAL DISPLACEMENT OF THE PIPE AT NON-LOCK-IN AT L/8

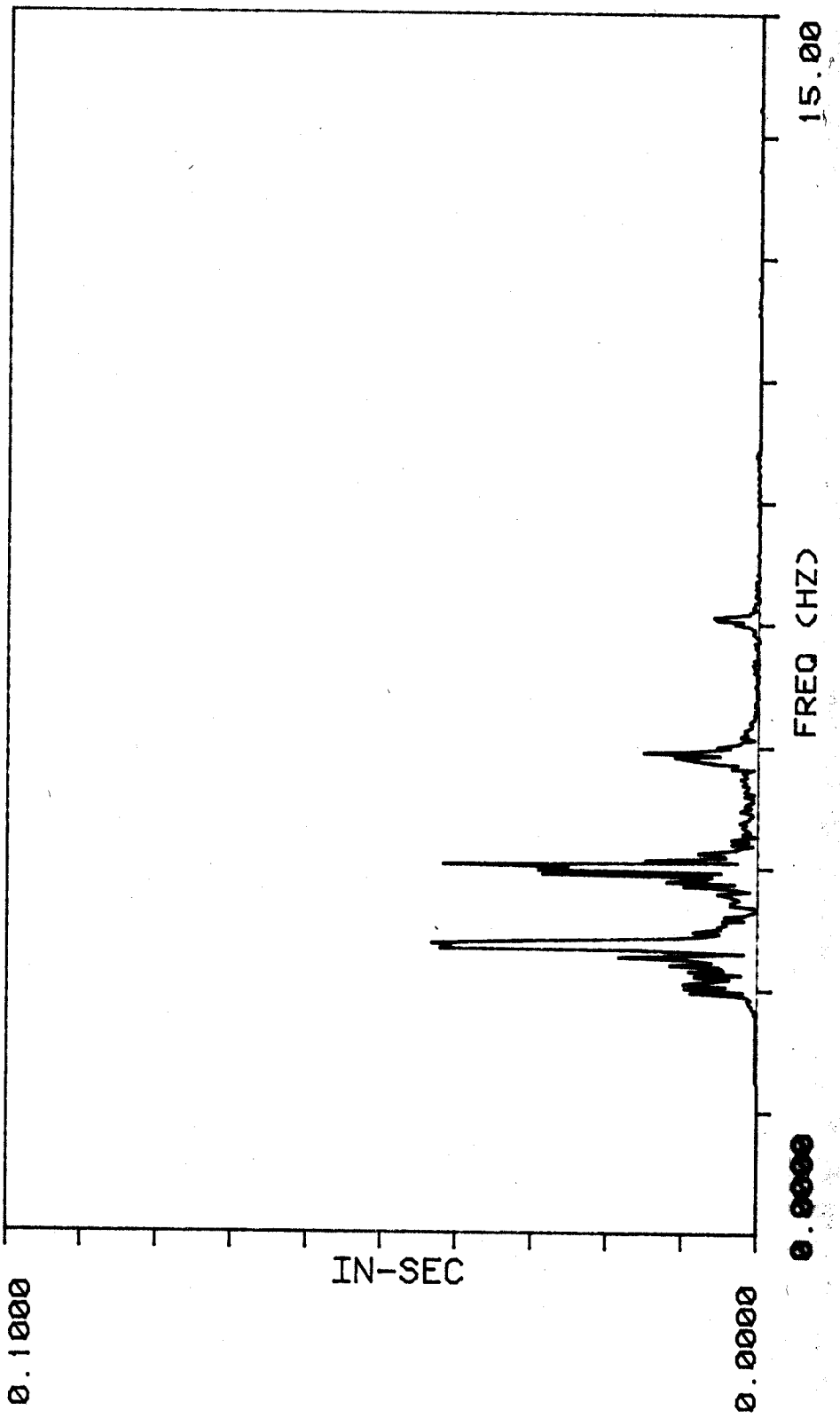

FIG.23 FFT OF THE HORIZONTAL DISPLACEMENT IN FIG.22

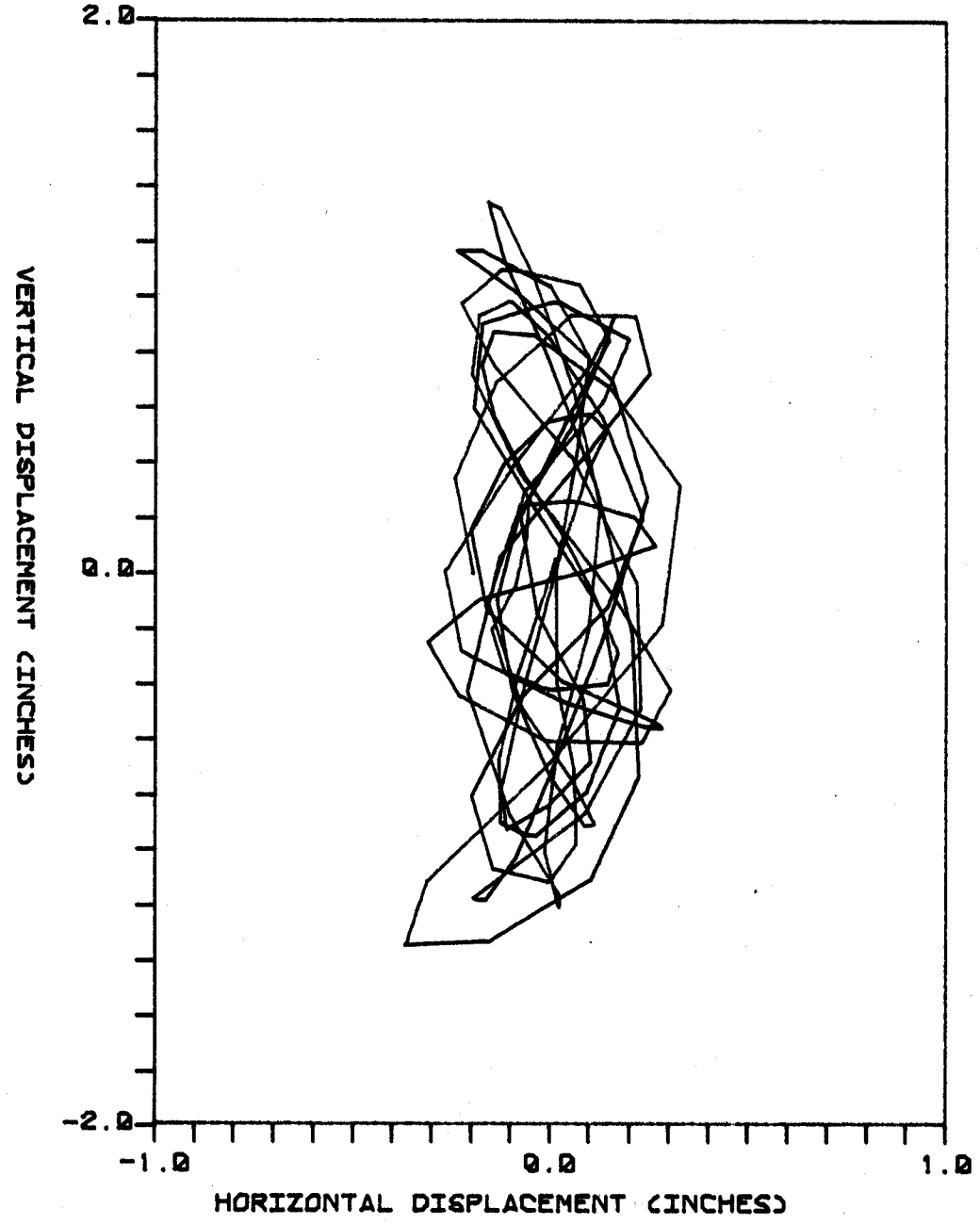

FIG.24 TWO-DIMENSIONAL MOTION TIME HISTORY OF THE PIPE AT NON-LOCK-IN AT L/8

for complete 2 1/2-hour data acquisition cycles were calculated for the pipe, bare cable, faired cable and a cable with lumped masses. The RMS data were calculated by a moving average whose window was 8.53 seconds in length. The equation used was:

$$RMS = \sqrt{\frac{1}{N} \sum_{n=1}^{N} X^2[n]} \qquad (4.3.1)$$

where N is 256 points and represents a time window of 8.53 seconds at a sampling rate of 30 HZ. These results are presented in Figs. 25 to 28, along with linear moving average values of drag coefficient and current speed. The displacement data are taken from location 1/6 L for the pipe and the bare cable, from location 3/4 L for the cable with lumps and from location 2/5 L for the faired cable. These are raw RMS displacements at the specified location and have not been corrected for mode shape. Over the 2 1/2-hour test, some periods correspond to lock-in responses, and others to non-lock-in responses. As current speed falls within a lock-in range, a substantial increase of vertical and/or horizontal RMS displacement is observed. A corresponding plateau in the drag coefficient is also observed. A more complete analysis of the drag coefficient data is presented in the thesis by McGlothlin (8). In that reference an analysis of the errors in the drag coefficient calculation is presented. A note of caution is appropriate here, the drag coefficient data is least accurate at the very low-flow speeds near the end of each test run. The drag coefficient calculation requires division of drag force by velocity squared. At low speeds these are both small numbers. At one foot/second the error is approximately +15% dropping to + 10% at 2.5 feet/sec. The high spike in the beginning of the drag coefficient record in Figure 25 is due to a piece of seaweed on the cable and should be disregarded.

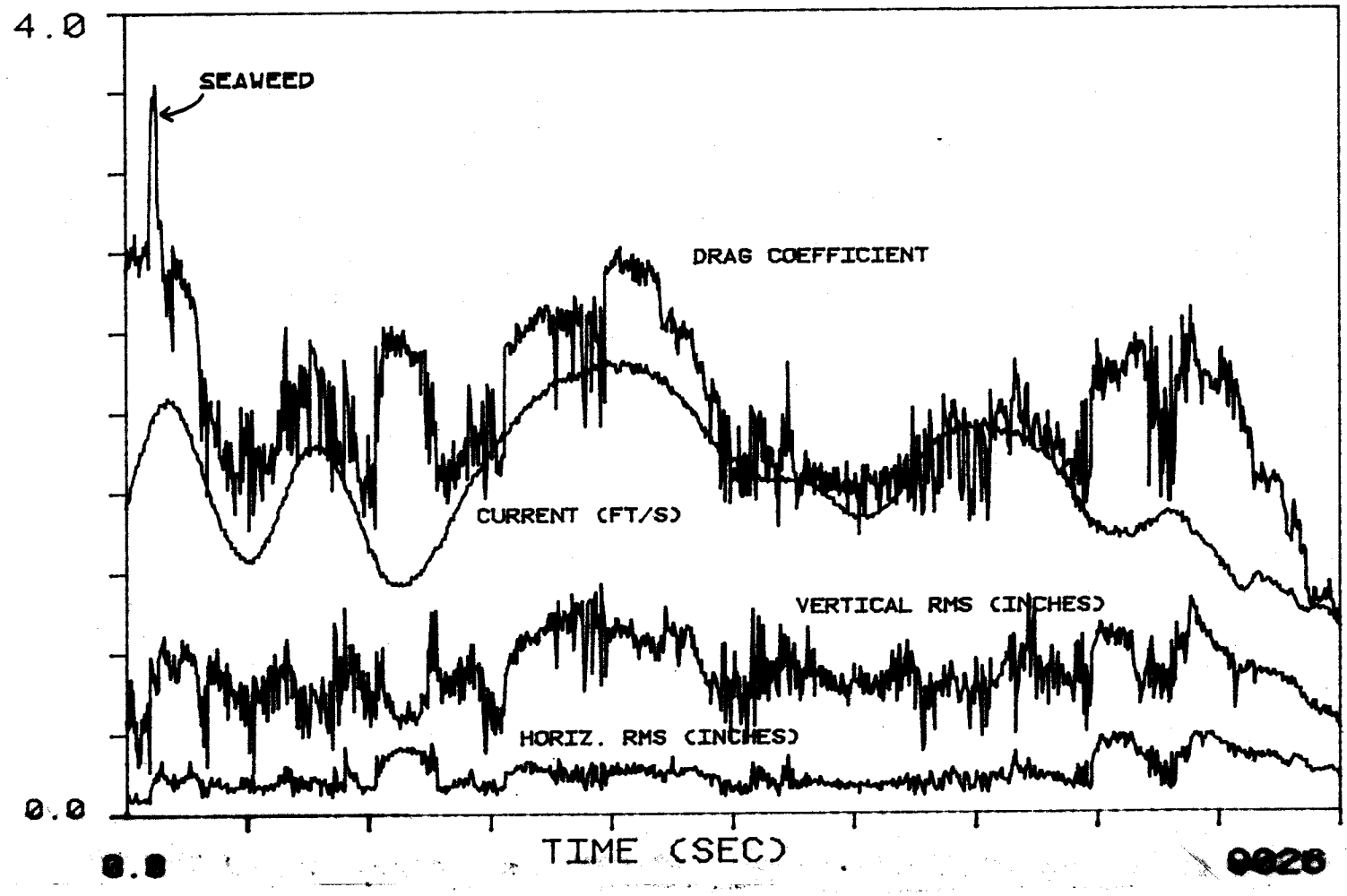

FIG. 25 2 1/2-HOUR RECORD OF THE DISPLACEMENT, CURRENT AND DRAG COEFFICIENT FOR THE PIPE AT L/6

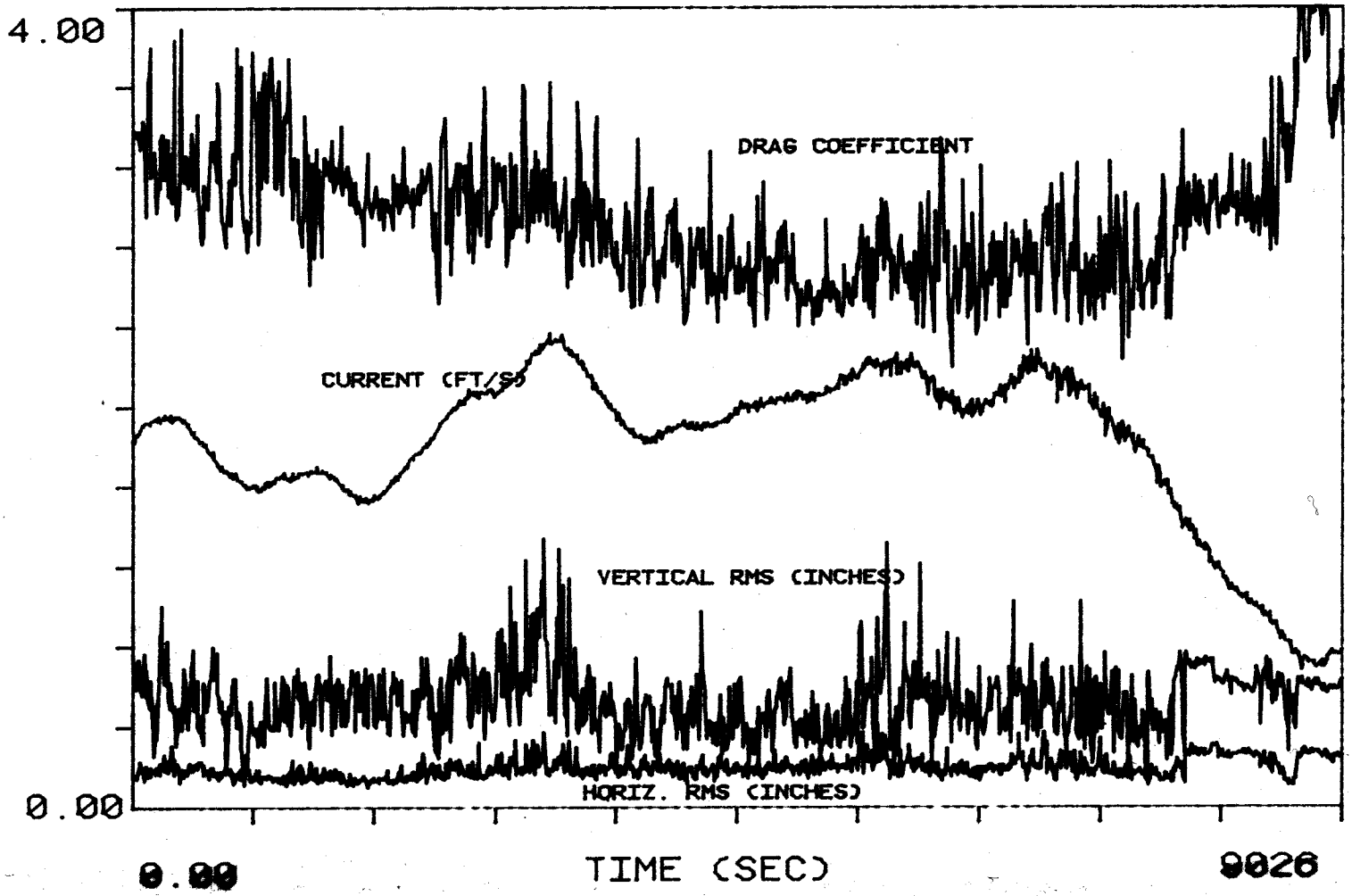

FIG.26 2 1/2-HOUR RECORD OF THE DISPLACEMENT, CURRENT AND DRAG COEFFICIENT FOR THE BARE CABLE AT L/6

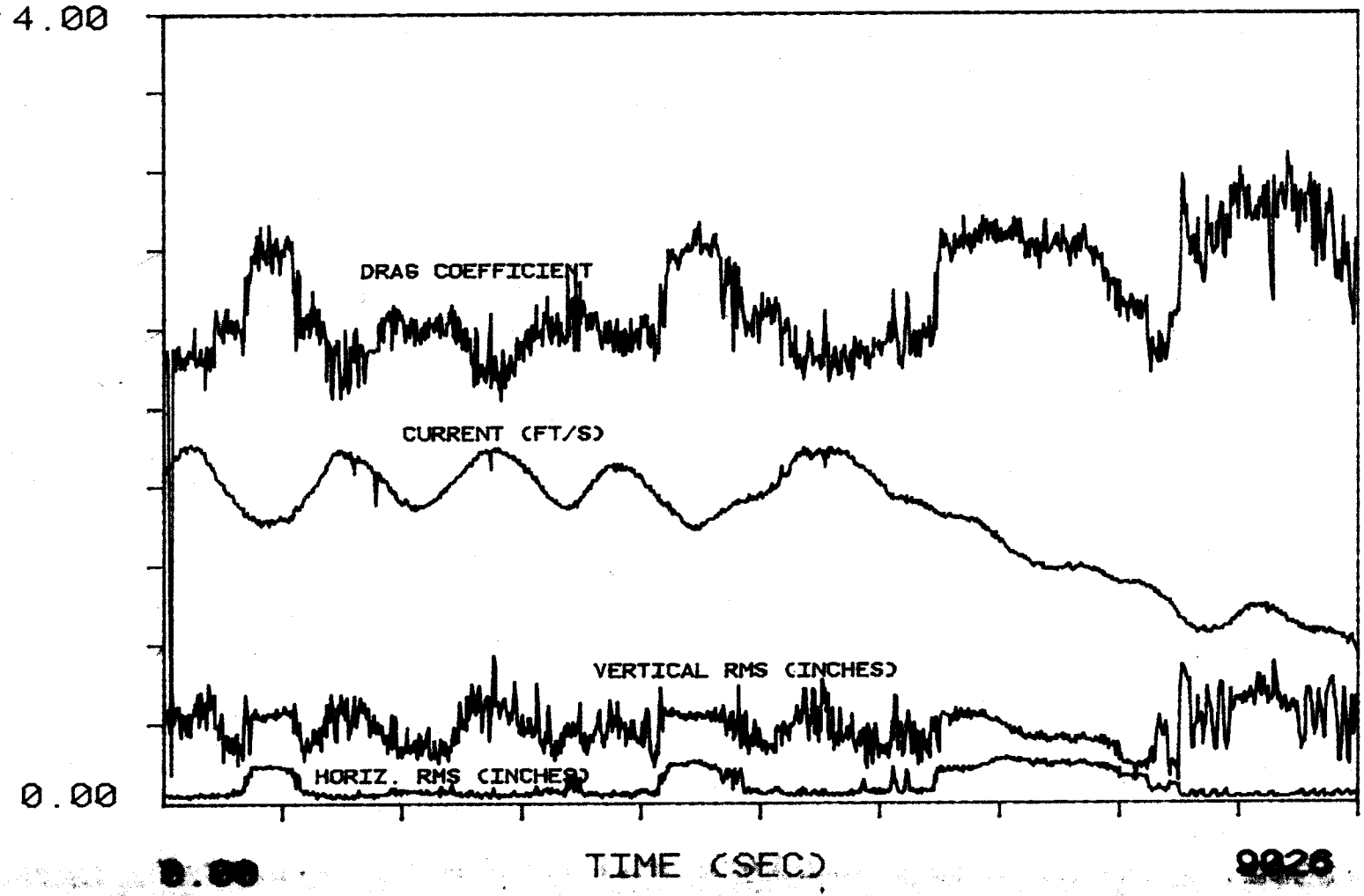

FIG.27 2 1/2-HOUR RECORD OF THE DISPLACEMENT, CURRENT AND DRAG COEF. AT 3L/4 FOR THE CABLE WITH 2 LIGHT (L/6, L/2) AND 4 HEAVY (L/3, 5L/8, 3L/4, 7L/8) LUMPED MASSES

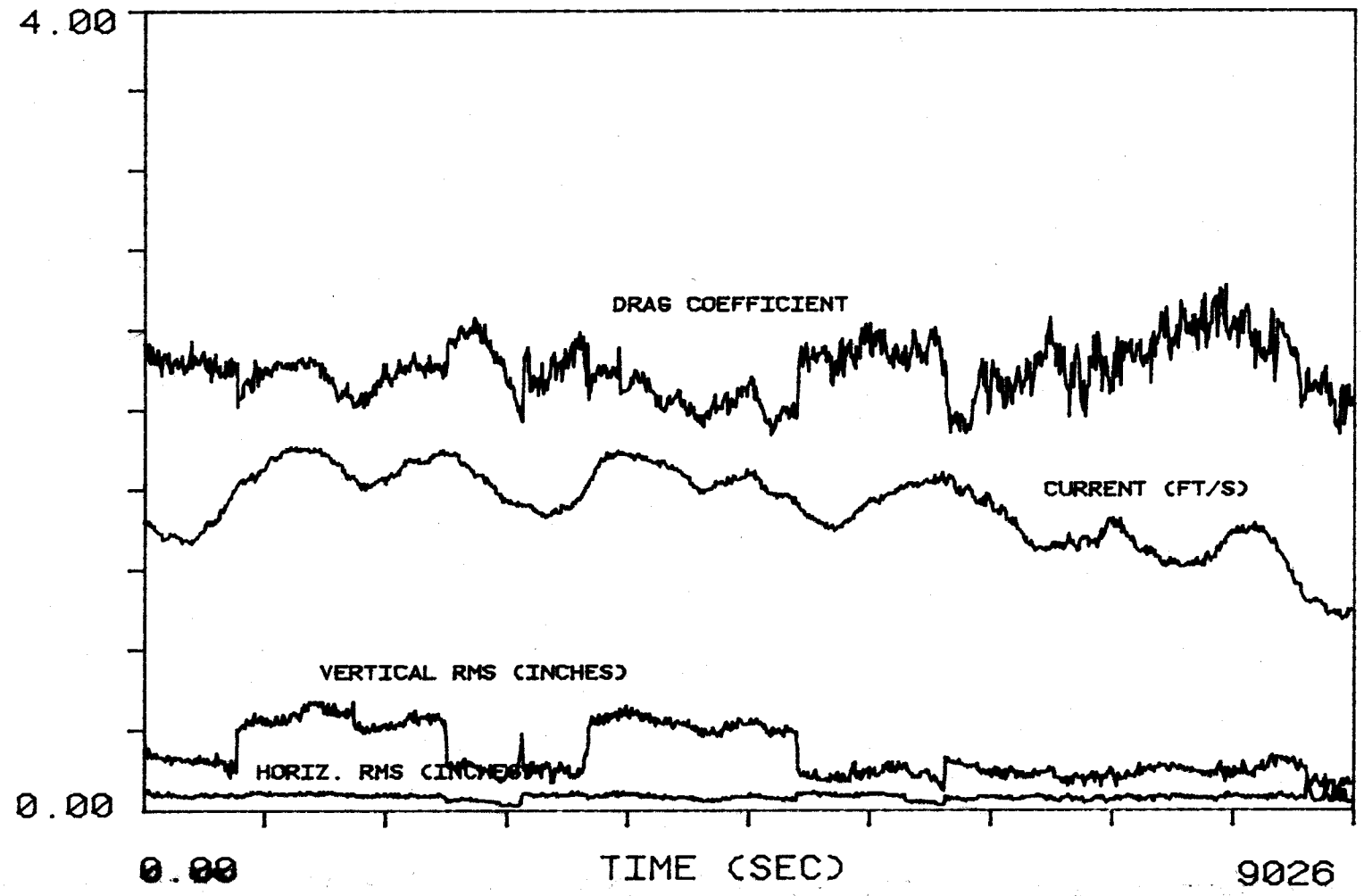

FIG. 28 2 1/2-HOUR RECORD OF DISPLACEMENT, CURRENT AND DRAG COEFFICIENT FOR THE FAIRED CABLE AT 2/5 L